Implementation of improved parameterization of terrestrial flux in WRF-VPRM improves the simulation of nighttime CO_2 peaks and a daytime CO_2 band ahead of a cold front

Xiao-Ming Hu[1], Sharon M. Gourdji[2], Kenneth J. Davis[3,4], Qingyu Wang[5], Yao Zhang[6], Ming Xue[1], Sha Feng[3], Berrien Moore[7], and Sean M. R. Crowell[7]

[1]Center for Analysis and Prediction of Storms, University of Oklahoma, Norman, Oklahoma 73072, USA
[2]National Institute of Standards and Technology, Gaithersburg, MD 20899, USA
[3]Department of Meteorology and Atmospheric Science and [4]Earth and Environmental Systems Institute, The Pennsylvania State University, University Park, PA 16802, USA
[5]School of Meteorology, University of Oklahoma, Norman, Oklahoma 73072, USA
[6]Department of Environmental Engineering, Columbia University, New York, NY 10027, USA
[7]GeoCarb Mission, University of Oklahoma, Norman, Oklahoma 73072, USA

Submitted to *Journal of Geophysical Research-Atmospheres*

on 12/3/20 11:36 PM

Corresponding author address:
Dr. Xiao-Ming Hu
Center for Analysis and Prediction of Storms
University of Oklahoma
Norman, Oklahoma 73072, USA
Email: xhu@ou.edu
Phone: (405) 325- 0402

Key Points

1. A new terrestrial ecosystem respiration parameterization accounting for vegetation index, water stress, and a nonlinear temperature dependence is implemented in WRF-VPRM to improve the simulation of both respiration and GPP.
2. The daytime bands of elevated CO_2 mole fractions ahead of cold fronts form in part due to the accumulation of nighttime respiration; hence the new VPRM improves performance.
3. Cloud-shading induced perturbation of photosynthesis cannot explain the CO_2 band immediately ahead of the surface cold front on 4 August 2016 because of its small magnitude and lagging behind the front.
4. Biological CO_2 clearly dominates the lower tropospheric CO_2 mole fraction patterns on the synoptic scale, with cross-frontal variations of more than 30 ppm for photosynthesis and respiration.

Abstract

Enhanced CO_2 mole fraction bands were often observed immediately ahead of cold front during the Atmospheric Carbon and Transport (ACT)-America mission and their formation mechanism is undetermined. Improved understanding and correct simulation of these CO_2 bands are needed for unbiased inverse CO_2 flux estimation. Such CO_2 bands are hypothesized to be related to nighttime CO_2 respiration and investigated in this study using WRF-VPRM, a weather-biosphere-online-coupled model, in which the biogenic fluxes are handled by the Vegetation Photosynthesis and Respiration Model (VPRM). While the default VPRM satisfactorily parameterizes gross ecosystem exchange, its treatment of terrestrial respiration as a linear function of temperature was inadequate as respiration is a nonlinear function of temperature and also depends on the amount of biomass and soil wetness. An improved ecosystem respiration parameterization including enhanced vegetation index, a water stress factor, and a quadratic temperature dependence is incorporated into WRF-VPRM and evaluated in a year-long simulation before applied to the investigation of the frontal CO_2 band on 4 August 2016. The evaluation shows that the modified WRF-VPRM increases ecosystem respiration during the growing season, and improves model skill in reproducing nighttime near-surface CO_2 peaks. A nested-domain WRF-VPRM simulation is able to capture the main characteristics of the 4 August CO_2 band and informs its formation mechanism. Nighttime terrestrial respiration leads to accumulation of near-surface CO_2 in the region. As the cold front carrying low-CO_2 air moves southeastward, and strong photosynthesis depletes CO_2 further southeast of the front, a CO_2 band develops immediately ahead of the front.

1. Introduction

An enhanced CO_2 mole fraction band was often observed immediately ahead of cold fronts during the Atmospheric Carbon and Transport (ACT)-America mission (Pal et al., 2020). Correct simulation of the gradients of CO_2 across cold fronts and understanding of the formation mechanisms are needed for accurate estimation of regional CO_2 budget (Chan et al., 2004; Hurwitz et al., 2004; Lee et al., 2012; Pal et al., 2020; Parazoo et al., 2008). Improved understanding of atmospheric constituents including CO_2 ahead of fronts may also help explain air pollution events sometimes found ahead of fronts (Hu et al., 2019a) since CO_2 and pollutants are sometimes co-emitted (Brioude et al., 2013; Brioude et al., 2012; Konovalov et al., 2014; Lindenmaier et al., 2014; Reuter et al., 2019; Turnbull et al., 2011; Wunch et al., 2009; Yang et al., 2019a). These CO_2 bands were previously briefly examined using WRF-VPRM, a weather-biosphere-online-coupled model, in which the terrestrial fluxes are handled by the Vegetation Photosynthesis and Respiration Model (VPRM) while the Weather Research and Forecast (WRF) model (Skamarock et al., 2008; Skamarock & Klemp, 2008) is used to simulate atmospheric flows and CO_2 transport and diffusion. These previous WRF-VPRM simulations were able to capture the existence of the CO_2 bands during the ACT-America mission (Hu et al., 2020a). However substantial bias in terms of CO_2 magnitude existed, which appeared related to underestimation of diurnal variation of CO_2, particularly nighttime CO_2 peaks (Li et al., 2020; Wang et al., 2020). Other studies also implied that VPRM and WRF-VPRM tended to underestimate nighttime CO_2 fluxes (Dayalu et al., 2018; Lopez-Coto et al., 2017) and concentration (Park et al., 2020). Nighttime CO_2 biases were not extensively examined previously. Many previous regional CO_2 studies focused on daytime boundary layer CO_2, while nighttime CO_2 was less studied (Parazoo et al., 2008), likely because of two factors: 1, nighttime CO_2 simulations are less trusted because of uncertainties in the

parameterization of the nighttime boundary layer and terrestrial respiration fluxes; 2, many remote-sensing and in-situ (such as aircraft) CO_2 observations are only available during daytime (Crevoisier et al., 2010; Pal et al., 2020; Sweeney et al., 2015).

Terrestrial ecosystem respiration in simple empirical modeling systems such as VPRM is often parameterized as a function of temperature, thus not accounting for factors such as soil moisture and substrate available for heterotrophic respiration (Ai et al., 2020; Buchmann, 2000; Fang & Moncrieff, 2001; Lloyd & Taylor, 1994; Raich et al., 2002; Schubert et al., 2010). VPRM simulates the Net Ecosystem Exchange (NEE) of CO_2 through separate parameterizations for ecosystem respiration (ER) and Gross Ecosystem Exchange (GEE) (Mahadevan et al., 2008)

$$\mathrm{NEE} = \mathrm{ER} + \mathrm{GEE} \quad (1)$$

$$\mathrm{ER} = \alpha \times T + \beta \quad (2)$$

$$\mathrm{GEE} = \lambda \times T_{scale} \times W_{scale} \times P_{scale} \times FAPAR_{PAV} \times PAR \times \frac{1}{1+\frac{PAR}{PAR_0}} \quad , \quad (3)$$

where α and β are parameters used to model ecosystem respiration as a function of temperature T, λ is the maximum light use efficiency, T_{scale}, W_{scale}, and P_{scale} account for effects of temperature, water stress, and leaf age on photosynthesis, respectively, $FAPAR_{PAV}$ is the Fraction of Photosynthetically Active Radiation (PAR, μmol m^{-2} s^{-1}) absorbed by the photosynthetically-active portion of the vegetation, which roughly equals the Enhanced Vegetation Index (EVI), and PAR_0 is the half-saturation value. This version of VPRM (Mahadevan et al., 2008) and the corresponding parameters previously calibrated off-line using eddy covariance tower data over North America (Hilton et al., 2016) were implemented into WRF-VPRM to examine spatiotemporal variation of CO_2 over the contiguous U.S. (Hu et al., 2020b) and northeastern China (Li et al., 2020). While Eq. (3) is a light-use efficiency algorithm commonly used to simulate GEE (Dong et al., 2015; Wagle et al., 2014; Zhang et al., 2016a; Zhang et al., 2016b; Zhang et al., 2018; Zhang et al., 2017), respiration (Eq. 2), is considerably simpler than parameterizations of

ecosystem respiration in more complex, process-based models. Ecosystem respiration depends not only on temperature but also on other factors such as soil moisture (Davidson et al., 1998; Murayama et al., 2003; Rey et al., 2002) and the mass of leaf and stem of biomes (proxy of plant productivity) that can be roughly represented by EVI (Guan et al., 2006). The leaf and stem respiration (which is the dominant contributor to autotrophic respiration) was observed to account for about 27%-52% of the total ecosystem respiration on annual average, with a higher percentage during summer (Guan et al., 2006; Tang et al., 2008). Biogeochemical models like Carnegie Ames Stanford Approach (CASA) (Zhou et al., 2020) and Simple Biosphere Model (SiB4) (Haynes et al., 2019) track carbon pools, and simulate respiration as a function of the carbon pool size, along with pool-specific litter decay rates and environmental controlling factors. Other studies (Loranty et al., 2011) attempted to include plant productivity in ecosystem respiration parameterization by making respiration a function of leaf area index. A better respiration parameterization is warranted for improving WRF-VPRM.

Recently an improved terrestrial respiration parameterization in VPRM has been developed by incorporating EVI, water stress scaling factor (W_{scale}) and its interactions with temperature to capture soil moisture effects, and a quadratic dependence on surface air temperature (T in ºC) (Gourdji et al., 2020):

$$ER = \beta + \alpha_1 \cdot T + \alpha_2 \cdot T^2 + \gamma \cdot EVI + k_1 \cdot W_{scale} + k_2 \cdot W_{scale} \cdot T + k_3 \cdot W_{scale} \cdot T^2 \quad (4)$$

The parameters in this improved VPRM (Eq. 3 and 4) were calibrated with comprehensive flux tower data. Preliminary evaluation showed that this improved parameterization leads to better prediction of diurnal and monthly variation of CO_2 fluxes and concentration (Gourdji et al., 2020). This improved respiration parameterization is implemented into WRF-VPRM in this study and its performance over the contiguous United States (CONUS) is evaluated in 2016, particularly in

terms of reproducing nighttime boundary layer CO_2 at six NOAA towers (see their locations in Fig. 1), where hourly in-situ boundary layer CO_2 data are available in both daytime and nighttime. High-resolution simulations with this improved WRF-VPRM is further used to examine the CO_2 band ahead of the cold front on 4 August 2016 observed during the ACT-America aircraft field campaign, a case well documented previously using observations (Pal et al., 2020) and simulations.

2. Modeling approach and evaluation data

2.1 Brief description of VPRM improvement

The respiration parameterization of Eq. (4) is implemented into WRF-VPRM. While in the GEE calculation (Eq. 3), W_{scale} considers water stress effect using a function of Land Surface Water Index (LSWI):

$$W_{scale}(GEE) = \frac{1+LSWI}{1+LSWI_{max}} \quad (5)$$

following earlier VPRM development studies (Mahadevan et al., 2008; Xiao et al., 2004), W_{scale} used for ER calculation adopts

$$W_{scale}(ER) = \frac{LSWI-LSWI_{min}}{LSWI_{max}-LSWI_{min}} \quad (6)$$

proposed by Matross et al. (2006) for relatively-more water-limited region, because Eq. (6) leads to a larger variation of W_{scale} between different seasons with different water stresses. Eq. 6 was previously used for GEE calculation in grass and shrubs, but we change it to Eq. 5 to better match early growing season uptake in these ecosystems (Gourdji et al., 2020).

To maintain minimal terrestrial respiration in presence of low temperature in winter months and account for the fact that soil temperature is higher than air temperature during winter, the temperature (in ^{o}C) used in Eq. (4) is adjusted to

$$T = (T_a - T_{crit}) \cdot T_{scale2} + T_{crit} \quad (7)$$

159 when the air temperature T_a is lower than T_{crit}. The VPRM parameters (GEE and respiration
160 parameters in Eq. 3, 4, and T_{scale2} and T_{crit} in Eq. 7) for each vegetation type are summarized in
161 Table 1, and were calibrated by Gourdji et al., (2020) using AmeriFlux data
162 (*https://ameriflux.lbl.gov/sites*). Respiration parameters were first calibrated using nighttime data,
163 and then daytime respiration were computed, and daytime GEE were separated out, which was
164 subsequently used to optimize GEE parameters. This is a different optimization procedure than
165 originally formulated by Mahadevan et al (2008), where 24 hours of hourly NEE are used to
166 simultaneously optimize GEE and respiration parameters. The new optimization procedure results
167 in a larger magnitude of both respiration and GEE, and hence the diurnal cycle of NEE, by
168 separately fitting respiration and GEE parameters to night and day-time observations respectively.
169 A more detailed description of the improved VPRM and parameter calibration can be found in
170 Gourdji et al. (2020), although parameters for western shrubs and grasslands were optimized
171 separately for the simulations presented in this study, given that Gourdji et al. (2020) focuses on
172 estimating fluxes in eastern North America.
173
174 **2.2 Configurations of WRF-VPRM simulations and episode description**
175
176 Two kinds of WRF-VPRM simulations, referred to as year-long and episodic, are
177 conducted. A single-domain, one year WRF-VPRM downscaling simulation is conducted over
178 the CONUS domain at a 12-km grid spacing in 2016 to examine the updated VPRM performance
179 over a full year. Following the year-long run, nested-domain episodic WRF-VPRM simulations
180 are conducted for 4 August 2016 to examine the formation mechanism of the CO_2 band ahead of
181 the cold front at a higher horizontal resolution, with an inner nested domain covering the northern
182 Great Plains at a 4 km grid spacing (see domain configuration in Fig. 1).

183 The year-long WRF-VPRM simulation follows the configuration of our previous
184 downscaling study (Hu et al., 2020b), with the NCEP/DOE R2 data (Kanamitsu et al., 2002)
185 providing meteorological initial and boundary conditions and the CT2017 global simulation 3°×2°
186 outputs (Peters et al., 2007) providing CO_2 initial and boundary conditions. Anthropogenic CO_2
187 emissions are taken from the 0.1°×0.1° Open-Data Inventory for Anthropogenic Carbon dioxide
188 (ODIAC) (Oda et al., 2018) version 2018 and ocean CO_2 fluxes are taken from climatological
189 monthly values derived by Takahashi et al. (2009). Using ODIAC led to a better CO_2 simulation
190 than using Emission Database for Global Atmospheric Research (EDGAR) in Hu et al. (2020b).
191 Selected major physics parameterization schemes within WRF include the Dudhia shortwave
192 radiation scheme (Dudhia, 1989), the rapid radiative transfer model (RRTM) (Mlawer et al., 1997)
193 for longwave radiation, the Noah land surface model (Chen & Dudhia, 2001), the Grell-3 cumulus
194 scheme (Grell & Devenyi, 2002), the Morrison microphysics scheme (Morrison et al., 2009), and
195 the Yonsei University (YSU) planetary boundary layer (PBL) scheme (Hong et al., 2006).
196 Selection of PBL schemes is critical for accurate simulation of lower tropospheric CO_2 vertical
197 distribution (Ballav et al., 2016; Diaz-Isaac et al., 2018) and CO_2 accumulation ahead of cold fronts.
198 The YSU scheme has been shown to perform well for both daytime and nighttime at the 12 and 4
199 km grid spacings used in this study (e.g., Hu et al., 2012; Hu et al., 2013; Hu et al., 2010b; Hu et
200 al., 2019b; Yang et al., 2019b). The YSU scheme is a nonlocal scheme with explicit treatment of
201 entrainment fluxes, which was shown to be critical to reproducing convective boundary layer
202 structures (Hu et al., 2010b; Hu et al., 2019b) and achieve a better performance than some local
203 schemes such as the Mellor–Yamada–Janjic (MYJ) scheme (Wang et al., 2016). For stable
204 boundary layer, an update in stability function in 2013 led to a better YSU performance in terms
205 of reproducing nighttime profiles of both meteorological and chemical variables, particularly over

206 the Great Plains (Hu et al., 2013). The model domain has 47 vertical layers extending from the
207 surface to 10 hPa with 21 layers in the lower 2 km above the ground to resolve boundary layer
208 processes. The WRF-VPRM downscaling simulation ran continuously from January 1 to
209 December 31, 2016, adopting the spectral nudging technique (Gomez & Miguez-Macho, 2017;
210 Otte et al., 2012; Vincent & Hahmann, 2015) to ensure that the large scale flows do not deviate
211 from the driving NCEP/DOE R2 data, following our previous downscaling studies (Hu et al.,
212 2020b; Hu et al., 2017; Hu et al., 2018). Such long-term regional simulations refine global model
213 simulation (CT2017 in this case) and improve the general accuracy of simulation by better
214 resolving local forcing and atmospheric processes, and are commonly referred to as dynamic
215 downscaling.

216 The nested-domain simulations for 4 August 2016 examine the formation mechanism of
217 the CO_2 band ahead of the cold front on the nested 4 km grid. During the selected episode, a
218 surface cold front that formed on 3 August moved southeastward quickly to central Nebraska until
219 12 CST (18 UTC) 4 August when it slowed down (Pal et al., 2020). Along the front, scattered
220 light clouds were present and at some isolated points/time there were large thunderstorms, e.g., at
221 Lincoln after landing of ACT research flight. OCO-2 XCO_2 data indicate a transition of low XCO_2
222 to high XCO_2 across the front (Fig. 1c). But due to the interference of clouds, OCO-2 could not
223 detect the detailed gradient across the front (Bell et al., 2020; O'Dell et al., 2018). Lower
224 troposphere measurements from the ACT-America flight campaign reveal an enhanced CO_2 mole
225 fraction band (~50 km wide) immediately ahead of the cold front with the cross-frontal CO_2
226 contrast as high as 30 ppm (Pal et al., 2020). Note ppm is equivalent to μmol/mol. These CO_2
227 bands formed likely due to a few factors including horizontal and vertical transport, and reduced
228 photosynthetic uptake caused by clouds (Chan et al., 2004; Hu et al., 2020a; Lee et al., 2012). The

finer horizontal and vertical resolutions used in this study can better resolve small-scale processes and shallow surface layers than earlier studies using coarse resolutions (e.g., Chan et al., 2004), which is critical for reproducing the formation of the narrow CO_2 bands. To diagnose the CO_2 band, in addition to the fully coupled control run, two sensitivity simulations (summarized in Table 2) are conducted, in which clear-sky radiation is used to drive VPRM and the Noah land surface model, respectively. These sensitivity simulations are designed to isolate the impact of cloud shading on terrestrial CO_2 fluxes and surface energy balance, respectively, and the subsequent impact on frontal CO_2 structures.

2.3 Description of Observations

2.3.1 NOAA Tall Towers

Hourly data from six NOAA tall towers over central and eastern half of US, i.e., WLEF Tower (LEF), Argyle, Maine Tower (AMT), West Branch, Iowa (WBI), South Carolina Tower (SCT), Boulder Atmospheric Observatory (BAO), and WKT Tower (WKT), are used to evaluate simulated CO_2 profiles in the continental boundary layer during both daytime and nighttime. The measurements at BAO were discontinued on 26 July 2016. More detailed description of those towers can be found at https://www.esrl.noaa.gov/gmd/ccgg/insitu/.

2.3.2 Atmospheric Carbon and Transport (ACT)-America data

The ACT-America mission was conducted to improve the understanding of sources and sinks of CO_2 at regional scale (~10^6 km^2) and transport of greenhouse gases by weather systems in midlatitudes. During the mission, two aircraft (NASA Wallops C130 - Hercules and NASA Langley B200 – King Air) were deployed over the eastern half of the continental U.S. during 2016-2019, to measure meteorological variables and gas species including CO_2 and CH_4 across a variety of weather conditions in both the boundary layer and the free troposphere (Davis et al., 2018;

Digangi et al., 2018). Airborne CO_2 were measured using a PICARRO 2401-m analyzer calibrated with gas standards traceable to the WMO scale. The ACT-America flight data on 4 August 2016 (see flight track of B200 in Fig. 1) are used in this study to evaluate the CO_2 simulation with the updated WRF-VPRM and to examine the CO_2 band ahead of the cold front.

3. Results

3.1 Evaluation of year-long CO_2 downscaling simulation with tower data

The year-long WRF-VPRM downscaling simulation is conducted mainly to examine the performance of the updated VPRM, particularly in terms of reproducing nighttime boundary layer CO_2 peaks, because nighttime CO_2 was found to contribute substantially to the daytime CO_2 bands ahead of cold fronts (Hu et al., 2020a). Note that the effect of simulated CO_2 variations on radiation and subsequent weather is not considered in current WRF-VPRM (such effect should be much smaller than meteorological conditions such as clouds, atmospheric temperature and water vapor distributions (Houghton & Moir, 1977)). Instead, a climatological CO_2 mole fraction (379 ppm) is used in the radiation scheme. Thus, updates in VPRM do not affect the simulated meteorological fields, which are essentially the same as those reported in Hu et al. (2020b). Comprehensive evaluation conducted in Hu et al. (2020b) concluded that the downscaled meteorological fields are sufficiently accurate to drive online coupled VPRM and subsequent CO_2 simulation.

The updated VPRM predicts enhanced respiration during growing season, partially due to added dependence on EVI. While a more detailed evaluation of VPRM fluxes can be found in a companion paper (Gourdji et al., 2020), CO_2 fluxes at an AmeriFlux site (US-Ne3, see its location in Fig. 1) near the B200 flight track are evaluated in Fig. 2. During non-growing season, both model and observations show minimal NEE except observations show occasional spikes. During

growing season at this crop site (July, August, September), both negative and positive CO_2 fluxes are enhanced, indicating daytime NEE and nighttime ER, respectively. The previous version of VPRM with Eq. (2) underestimates growing season NEE and ER (Fig. 2a,c). With the modified ER parameterization (Eq. 4) and newly calibrated parameters, the updated VPRM (referred to as VPRM_G in figure legends) predicts enhanced productivity with enhanced NEE during both daytime and nighttime during growing season, showing a better agreement with observations (Fig. 2b,d). The growing season mean bias of nighttime CO_2 fluxes is reduced from -4.2 to -0.2 μmol CO_2 m^{-2} s^{-1} at this site, which is a critical improvement to reproducing the daytime CO_2 bands ahead of cold front as will be discussed in section 3.2. Different from simulated fluxes, which represent the average flux over a 12×12 km^2 grid cell, observed fluxes represent the flux at the site and observed nighttime fluxes often show positive spikes (Fig. 2a,b) presumably due to instantaneous intermittent turbulence particularly during growing season (Aubinet, 2008). The median diurnal variation of CO_2 fluxes during growing season is evaluated in Fig. 2c,d, which further confirms that the new VPRM better captures the diurnal variation of fluxes relative to the old VPRM formulation. Examination of CO_2 fluxes at a grass site in Kansas close to the 4 August B200 flight track also indicates a better performance of the new VPRM (figure not shown).

Fluxes along with transport dictate the atmospheric CO_2 spatiotemporal variation. Simulated hourly CO_2 values at six NOAA tower sites are evaluated. Among the six sites, three northern sites, WBI (crop site) and LEF and AMT (mixed forest sites), show more pronounced seasonal variation of CO_2 (Fig. 3), indicating more pronounced seasonal cycle of productivity. The strong variation of hourly values in the growing season (Fig. 4) is due to enhanced diurnal variation of NEE relative to non-growing season. Detailed hourly variation of CO_2 in first half of July is shown in Fig. 5, illustrating intense diurnal variation with nighttime CO_2 peaks (grey shading) and

afternoon CO_2 minima (no shading). Afternoon minimum CO_2 shows a prominent seasonal cycle with minimum in July-August at WBI crop site and in June-September at LEF, AMT mixed forest sites (Fig. 3), consistent with previous studies (Bakwin et al., 1998; Parazoo et al., 2008), indicating active terrestrial uptake in growing season during daytime. Note that mixed forest typically has a longer growing season than crop (Li et al., 2020). Such seasonal variation of afternoon minimum CO_2 also shows up in the aircraft boundary layer CO_2 data from NOAA Global Greenhouse Gas Reference Network (https://www.esrl.noaa.gov/gmd/ccgg/aircraft/) and the XCO_2 data recorded at Total Carbon Column Observing Network [TCCON] (Hu et al., 2020b), both of which only have daytime observations. Relatively-less-reported is the seasonal variation of nighttime CO_2 peaks/spikes (e.g., Bakwin et al., 1998; Davis et al., 2003), which increase significantly during growing seasons (Fig. 3). The increasing magnitude of nighttime CO_2 peaks/spikes during growing season is even larger than the decreasing magnitude of afternoon CO_2 minimum (Fig. 3).

For SCT and two grass sites, BAO, and WKT, the contrast between the non-growing season and growing season identified from time series of hourly CO_2 is not as clear as the crop and mixed forest sites, which is due to a smaller seasonal variation of local fluxes and location in the continent (Sweeney et al., 2015).

The updated VPRM showed improved performance compared to the previous version, particularly in terms of reproducing nighttime CO_2 peaks (Fig. 5). Overall, the underestimation of surface CO_2 is reduced, with 24-hour mean bias reducing from -5.3 ppm to -1.0 ppm at the six NOAA sites in 2016 (Table 3). During nighttime (22-06 CST) the mean bias is reduced from -9.4 ppm to -4.0 ppm (Table 5) while during the day (10-18 CST) the mean bias is changed from -1.1 ppm to 1.6 ppm (Table 4). The nighttime mean bias remains most prominent at two mixed forest

326 sites, AMT (-10.4 ppm) and LEF (-4.4 ppm) with the updated VPRM (Fig. 3, Table 5). At the
327 WBI crop site, nighttime mean bias reduced from -11.46 ppm to -4.2 ppm. The remaining bias at
328 night could be due to overestimated nighttime turbulent mixing (Hu et al., 2010b), as well as
329 underestimated nighttime respiration due to drainage and loss of measured flux at towers (Aubinet,
330 2008). These evaluations illustrate that the updated terrestrial respiration parameterization (i.e.,
331 Eq. 4) and the newly calibrated parameters (Table 1) have a much-improved skill to reproduce the
332 nighttime CO_2 peaks, as well as diurnal variation of near-surface CO_2, particularly during growing
333 season. Note that among the 6 NOAA towers, WBI is closest to the B200 flight track on 4 August
334 2016 and the flight track is mostly over the crop land category (Fig. 1a,b). Thus, significant
335 improvement of WRF-VPRM performance over the WBI crop site is likely to be particularly
336 beneficial to diagnose formation mechanism of the CO_2 band observed by B200 on 4 August.
337 In addition to terrestrial fluxes, the surface CO_2 concentration is dictated by boundary layer
338 vertical distribution. Boundary layer CO_2 profiles are examined in Figs. 6-8 to further diagnose
339 the CO_2 biases. During daytime (10, 14, 18 CST), CO_2 in the boundary layer is nearly well mixed,
340 except at 18 CST when CO_2 starts to accumulate near the surface at eastern sites, e.g., AMT and
341 SCT because these sites enter evening earlier comparing to western sites. The biases of these well-
342 mixed daytime profiles are minor, consistent with previous evaluation using daytime
343 measurements of boundary layer CO_2 from NOAA small aircraft and XCO_2 from TCCON (Hu et
344 al., 2020b).
345 Comparing to daytime, biases of nighttime boundary layer CO_2 are relatively-less-reported.
346 Through the night and the following early morning (22, 2, 6 CST), CO_2 from terrestrial respiration
347 keeps accumulating near the surface in presence of a stable boundary layer and near-surface
348 vertical gradients of CO_2 increase. Comparing to daytime, WRF-VPRM has more challenge to

reproduce the nighttime CO_2 peaks. The bias of near-surface CO_2 becomes prominent during nighttime. With increased nighttime respiration in the updated VPRM (Eq. 4), the nighttime bias is alleviated. However, the bias of early morning CO_2 at certain sites are still large. For example, at AMT, the bias reaches as large as >20 ppm at 2 CST and the bias quickly reduces to <10 ppm at 6 CST as the convective boundary layer starts to grow and photosynthesis becomes active at this eastern site, reducing surface-layer CO_2 peaks quickly (Fig. 6). At 6 CST, the bias of surface CO_2 at WBI and LEF reaches ~16 ppm and 10 ppm, and the biases at three other south sites, SCT, BAO, WKT are smaller. The median diurnal variations of CO_2 during growing season (Fig. 4) also illustrate the largest nighttime bias remains at AMT, WBI, and LEF. Future further improvement of simulating boundary layer CO_2 diurnal variation may focus on the biologically very productive sites such as WBI crop site and AMT, LEF mixed forest sites, and may benefit from co-located measurements of fluxes, mole fraction, and boundary layer meteorology (Davis et al., 2003; Yi et al., 2004; Yi et al., 2001).

3.2 Examination of the CO_2 band ahead of cold front on 4 August 2016

3.2.1 Analysis of ACT-America data and fully coupled WRF-VPRM control simulation

An important purpose of this study is to examine the cause of elevated CO_2 bands ahead of cold fronts, which appeared to be related to nighttime accumulation of near-surface CO_2 (Hu et al., 2020a). With improved capability to reproduce the nighttime CO_2 surface flux and mole fraction peaks with the updated VPRM, we seek to better diagnose the formation mechanism of the CO_2 bands. The CO_2 band ahead of the cold front on 4 August 2016 is examined with nested-domain WRF-VPRM simulations (see domain configuration in Fig. 1). In early morning (0600 CST), the model captures the stable boundary layer structure, as verified by routine sounding data at KLBF, KOAX, and KTOP in the vicinity of the ACT-America flight track on this day (Fig. 9).

At 1000 CST when C130 took off, the convective boundary layer grew up to ~ 700 m AGL, as indicated by the potential temperature profile measured by C130 (Fig. 9b). Nighttime accumulated CO_2 in the stable boundary layer was mixed in this early shallow convective boundary layer with a vertically constant mole fraction of ~418 ppm, about 14 ppm higher than the CO_2 mole fraction in the free troposphere above (Fig. 9a). The control WRF-VPRM simulation captures these boundary layer structures even though certain biases exist, including overestimation of boundary layer potential temperature by 2-3 K and underestimation of boundary layer CO_2 with a mean bias of ~5 ppm. During the morning, the cold front kept pushing southeastward bringing the low-CO_2 air mass (indicated by the OCO-2 XCO_2 data in Fig. 1c and aircraft data in Fig. 10a,b) into the region. Meanwhile, enhanced GEE over cropland around Lincoln and area east of Lincoln (partially due to large EVI in the region, Fig. 1a) reduced the boundary layer CO_2, leading to formation of a high CO_2 mole fraction band between west of Lincoln and leading edge of the cold front, which was detected by B200 at ~1230 CST when it flew westward and crossed the front (Fig. 10). The WRF-VPRM simulation captures the CO_2 gradient across the front in both the boundary layer and free troposphere (Fig. 10b) and the horizontal variation of boundary layer CO_2 mole fraction along the B200 flight track, including the CO_2 band immediately ahead of the cold front and west of Lincoln, albeit the band position is a little off (Fig. 10a,b), which is partially due to the time difference between observation and simulation. The CO_2 band was observed at ~1230 CST while the simulation is taken at 1200 CST in Fig. 10 (WRF outputted hourly).

Simulated individual components of CO_2 in the higher-resolution inner domain are examined to further diagnose the CO_2 band attribution. Total CO_2 are decomposed into background, biogenic, anthropogenic, and oceanic CO_2, which are tracked by individual tracer in WRF-VPRM. While biogenic, anthropogenic, and oceanic CO_2 are CO_2 accumulated from the

terrestrial biogenic fluxes, anthropogenic emissions and oceanic fluxes, background CO_2 is the CO_2 transported into the domain from the lateral boundary CO_2, which is derived from CT2017. Biogenic CO_2 can be further decomposed into respiration CO_2 and photosynthesis CO_2, which are CO_2 accumulated from transported ER and GEE, i.e., Eqs. (4) and (3). Among these components, oceanic CO_2 is negligible over the continent (Hu et al., 2020b) and therefore not shown here. The background CO_2 transported by the cold front has its origins from the northern boundary where CO_2 is low in summer (Hu et al., 2020b; Sweeney et al., 2015), thus southeastward penetration of background CO_2 carried by the cold front creates a step-function-like gradient (~6ppm difference) across the front, with a nearly constant CO_2 (~ 402 ppm) ahead of the cold front (Fig. 11b, 12b). The anthropogenic CO_2 includes a small contribution to CO_2 to the far east side along the B200 flight track, while it does not contribute to the CO_2 band immediately ahead of the cold front (Fig. 11d, 12d). The CO_2 enhancement band is mostly comprised of biogenic CO_2 (Fig. 11c), that is, accumulated from terrestrial biogenic fluxes, which contributes a ~15 ppm cross-front difference (Fig. 12c). The horizontal variation of biogenic CO_2 (Fig. 11c, 12c) matches the horizontal variation of total CO_2 (Fig. 11a, 12a) in terms of general trend.

Figure 12 also illustrates that updated VPRM significantly enhances the model capability to capture the CO_2 band ahead of the cold front. The previous version of VPRM, with a much weaker respiration given by Eq. (2), barely simulates any contribution to the cross-front CO_2 gradient from biogenic CO_2 at 12 CST, with only background CO_2 contributing a ~6ppm CO_2 gradient across the front. With a stronger respiration, updated WRF-VPRM simulates a dominating contribution from biogenic CO_2 (~15 ppm) to the cross-front CO_2 gradient, with certain biases still remaining including underestimating the peak concentration of the CO_2 band by ~8 ppm and overestimating the width of the CO_2 band.

To further delineate the effects of biogenic CO_2 fluxes, individual contribution history from respiration CO_2 and photosynthesis CO_2 during the morning of 4 August is examined in Fig. 13. In the early morning at 8 CST, respiration CO_2 ahead of the cold front is significant (~40 ppm) and does not show much variation along the B200 flight track (Fig. 13b). Photosynthesis CO_2 are enhanced (absolute value) over the cropland region with enhanced EVI (Fig. 1a) around Lincoln and area east of Lincoln (Fig. 13c). As a result of collective contribution of respiration and photosynthesis CO_2, biogenic CO_2 shows a band of enhanced mole fraction immediately ahead of the cold front (Fig. 13a). Through time, this CO_2 band is squeezed and pushed southeastward by the front, which was detected by B200 ~1230 CST (Fig. 13d). When the CO_2 band is pushed further into high GEE region east of Lincoln, stronger GEE (negative photosynthesis CO_2 contribution) gradually weakens the narrow CO_2 band immediately ahead of the cold front in the afternoon until it merges into the CO_2 background in the warm sector of the front (not shown).

The morning and noontime CO_2 band extends from the surface into the free troposphere (Fig. 10b, 11a) ahead of the cold front, which is related to nighttime convective transport of accumulated CO_2 from the nighttime stable boundary layer into the free troposphere (Fig. 14). The snapshots at 0200 CST shows significant updrafts and downdrafts ahead of the front associated with moist convection, which ejects the near-surface CO_2-rich and water vapor-rich air mass into the free troposphere. As a result, a weaker CO_2 band extends at least 3-4 km AGL (Fig. 11a). This may explain other CO_2 bands observed in the free troposphere by ACT-America flights. The moist convection in the region is more active during nighttime and weakens during the day on 4 August, which might be related to the diurnal variation of low-level jet (LLJ) over the Great Plains. On the night of 3-4 August, a strong LLJ is formed ahead of the cold front (not shown). The nighttime convection is presumably enhanced by convergence at the northern end of the LLJ over the

444 Northern Great Plains. Moist convective transport of chemical species has been reported to have
445 significant impacts on air quality (Barth et al., 2007; Hu et al., 2010a; Jiang et al., 2007; Langford
446 et al., 2010); it similarly impacts CO_2 transport and its budget in this case, as also shown by Penn
447 State simulations.
448
449 **3.2.2 Analysis of WRF-VPRM sensitivity simulations to examine cloud impacts**
450
451 Clouds associated with moist convection block shortwave radiation during the day, thus
452 affecting photosynthesis, and the land surface energy balance and eventually terrestrial CO_2 fluxes.
453 Two sensitivity simulations (summarized in Table 2) are conducted to examine the impact of
454 clouds on terrestrial fluxes and the frontal CO_2 band. In the clear-sky-photosynthesis simulation,
455 clear-sky radiation is used to drive VPRM. The difference between clear-sky-photosynthesis and
456 control runs shows the impact of clouds shading on terrestrial CO_2 fluxes (through Eq. 3), and
457 subsequent impact on frontal CO_2 structures. During the night of 3-4 August, moist convection
458 initially develops along the frontal boundary due to convergence. Through time, the convection
459 lags behind the surface cold front convergence line along the southwest end of the convection line
460 (Fig. 15). In the control simulation, reduced shortwave radiation due to cloud shading suppressed
461 GEE, thus leading to enhanced biogenic CO_2. However, the enhanced biogenic CO_2 due to cloud
462 shading (difference between control and clear-sky-photosynthesis) is minor (~2 ppm) comparing
463 to the total enhancement in biogenic CO_2 ahead of the leading edge of the front (~20 ppm) and
464 their position is not matching along the B200 flight track (Fig. 15). The storm weakens/shrinks
465 from 10 to 12 CST and does not move while the surface front keeps moving southeastward (Fig.
466 16). So the biogenic CO_2 due to cloud shading at the time remains lagging behind the front while
467 biogenic CO_2 during previous hours is transported southwesterly by the front, and the magnitude

468 remains ~2 ppm (Fig. 16). Thus, cloud shading barely contributes to the CO_2 band ahead of the
469 front observed by B200 in this case (Fig. 17).

470 At the northeast end of the convection line in the domain, the convection is at the leading
471 edge of the front and the contribution from cloud shading to CO_2 concentration enhancement is
472 more significant because biogenic activity is more vigorous (higher EVI), and convection is
473 stronger in the region. Thus, in this region, cloud shading contributes more to the CO_2 band ahead
474 of the front (Fig. 15, 16).

475 The impacts of clouds on CO_2 flux and mole fraction through the surface energy balance
476 is more complex. Since the nested-domain WRF-VPRM simulations start at 0000 UTC 4 August
477 (1800 CST), there is still daylight (shortwave radiation) in the first 2 hours of simulation during
478 early evening. Using clear-sky shortwave radiation to drive surface energy balance in the clear-
479 sky-surface-energy simulation initially leads to slightly higher temperature around clouds, which
480 later on provides perturbation for the strong moist convection during nighttime (not shown), and
481 the subsequent perturbation on CO_2 fields becomes quite non-linear, which can propagate through
482 the rest of simulation. The deep moist convection weakens during the day and cloud shading on
483 surface temperature becomes more linear. In the control simulation, cloud shading leads to lower
484 surface temperature compared to the clear-sky-surface-energy simulation (Fig. 18g). Despite a
485 nearly linear temperature response, its subsequent impact on CO_2 fluxes and mole fraction is
486 complex. Compared to the clear-sky-surface-energy simulation, lower temperature in the control
487 simulation results in lower respiration according to Eq. 4 and lower boundary layer height. Lower
488 respiration leads to lower biogenic CO_2, but lower boundary layer on the other hand leads to more
489 accumulation of respiration CO_2. The impact of lower surface temperature on photosynthesis is

also mixed depending on whether the ambient temperature is lower or higher than the optimal temperature (T_{opt}) because optimal temperature leads to the strongest GEE through the highest T_{scale} (Mahadevan et al., 2008). In the morning of 4 August, temperature in the nested 4 km domain varies from 5°C to 35°C, spanning both sides of the T_{opt} (25 °C and 18 °C) of two dominant vegetation types in the domain, i.e., crop and grass. Thus, the impact of reduced temperature due to cloud shading on NEE is mixed (Fig. 18h). Another likely impact of lower temperature behind the cold front is to slightly enhance the front penetration, which might explain the negative CO_2 difference between control and clear-sky-surface-energy along some portion of the front. Thus, with all these impacts, CO_2 difference between the control and clear-sky-surface-energy simulation has mixed results with both positive and negative values (Fig. 18i). Given the relatively small magnitude of these CO_2 difference (< 4 ppm), the elevated CO_2 mole fraction band ahead of the front is not alleviated by the impact of clouds on surface energy balance (Fig. 17).

4. Conclusions and Discussion

An enhanced CO_2 mole fraction band was often observed immediately ahead of cold fronts during the Atmospheric Carbon and Transport (ACT)-America mission and its cause is undetermined (Pal et al., 2020). Improved understanding and correct simulation of these CO_2 bands are needed for unbiased inverse CO_2 flux estimation. Such CO_2 bands are hypothesized to be related to nighttime CO_2 respiration and investigated in this study using WRF-VPRM, an online-coupled weather-biosphere model. While the original version of VPRM is mechanistically realistic and satisfactorily parameterizes gross ecosystem exchange with appropriate calibration, its treatment for terrestrial respiration, a linear dependence on temperature only, is inadequate to simulate ecosystem respiration that is nonlinear and also depends on biomass and soil wetness. In

512 this study, an improved terrestrial respiration parameterization that adds enhanced vegetation
513 index (EVI), water stress scaling factor (W_{scale}) and its interactions with temperature to capture
514 soil moisture effects, and a quadratic function of temperature (Gourdji et al., 2020) is incorporated
515 into the WRF-coupled VPRM and evaluated first in a year-long dynamic downscaling simulation
516 before being applied to investigate the CO_2 band ahead of a cold front on 4 August 2016.

517 The year-long downscaling simulation for 2016 is conducted over the contiguous United
518 States at a 12 km grid spacing with spectral nudging to help maintain consistency of large scale
519 flows with the driving reanalyses. Evaluations show that the improved WRF-VPRM simulates
520 a stronger respiration (and stronger GEE also), thus showing a better skill to reproduce
521 nighttime near-surface CO_2 peaks measured at six NOAA towers.

522 Nested-domain WRF-VPRM simulations including a 4-km inner domain covering the
523 Northern Great Plains are conducted for 4 August 2016 to examine the CO_2 band formation
524 mechanism. The control simulation is shown to be able to capture main characteristics of the
525 CO_2 bands, albeit with certain biases in magnitudes and/or locations. Nighttime terrestrial
526 respiration leads to accumulation of near-surface CO_2 in the region. As the cold front with low-
527 CO_2 air mass moves southeastward, together with strong photosynthesis depleting CO_2 further
528 southeast of the front, an enhanced CO_2 mole fraction band develops immediately ahead of the
529 front. Two sensitivity simulations are conducted to examine the impact of cloud shading on CO_2
530 attributions, using clear-sky radiation (i.e., neglecting cloud effects on radiation parameterization)
531 to drive VPRM and land surface energy balance respectively. Cloud shading is not found to
532 enhance or alleviate the CO_2 band observed by the ACT-America flight in this case because the
533 cloud shading-induced perturbation of biogenic CO_2 through radiative and surface temperature
534 effects is not significant and its location lags behind the surface cold front.

Though not shown here, a few other CO_2 bands ahead of cold front including the ones on Oct 18, 2017, and May 2, 2018, were also examined using WRF-VPRM simulations. Nighttime accumulation of respiration CO_2 is found to contribute substantially to these CO_2 bands, as in the case of 4 August 2016 (Hu et al., 2020a).

Parameterization of impact of radiation on photosynthesis in VPRM through Eq. (3) may be overly simplified. Some studies reported enhanced photosynthesis in presence of diffuse radiation. Such a process is not currently considered in VPRM. Nonetheless, this study illustrates the first-order effect of cloud shading on terrestrial CO_2 fluxes and CO_2 attribution around cold fronts.

This study finds that respiration fluxes contribute significantly to the CO_2 bands ahead of cold fronts. Further improvement of terrestrial respiration parameterization, particularly over biologically-very-active land covers, is warranted to improve CO_2 simulations in the vicinity of mesoscale/synoptic weather systems, which is critical to accurately estimate regional CO_2 budgets (Chan et al., 2004; Pal et al., 2020). In addition, transport/dispersion, particularly during nighttime, could also be improved to reduce CO_2 biases (Hu et al., 2013).

Acknowledgement. This study was supported by the Atmospheric Carbon and Transport (ACT)-America project through grant NNX17AG11G at OU and grant NNX15AG76G at Penn State. The ACT-America project is a NASA Earth Venture Suborbital 2 project funded by NASA's Earth Science Division. The last author was supported by NASA OCO-2 program under grant 80NSSC18K0896. Computations were performed at the San Diego Supercomputer Center (SDSC) through XSEDE allocation grant TG-ATM160014.

References are made to certain commercially available products in this paper to adequately specify the experimental procedures involved. Such identification does not imply recommendation or endorsement by the National Institute of Standards and Technology, nor does it imply that these products are the best for the purpose specified.

The reanalysis data set was downloaded from https://rda.ucar.edu/, and the CT2017 data were provided by NOAA ESRL, Boulder, Colorado, USA from the website at http://carbontracker.noaa.gov. Tomohiro Oda provided the $0.1^o \times 0.1^o$ Open-Data Inventory for

Anthropogenic Carbon dioxide (ODIAC) emissions. *Monthly ocean CO_2 fluxes are downloaded from https://www.ldeo.columbia.edu/res/pi/CO2/carbondioxide/pages/air_sea_flux_2000.html. ACT-America data (DOI 10.3334/ORNLDAAC/1593) is downloaded from* https://doi.org/10.3334/ORNLDAAC/1593. AmeriFlux data are downloaded from *https://ameriflux.lbl.gov/sites/site-search/*

Model data produced from this study have been archived at the oasis data server at the San Diego Supercomputer Center, `/oasis/projects/nsf/uok114/xhu2/CO2_and_otherGHG`

Table 1. Parameter values used in this study. Units for parameters are as follows: λ: μmol CO_2 $m^{-2}s^{-1}$/μmol PAR $m^{-2}s^{-1}$; β, λ, γ, k_1: μmol CO_2 $m^{-2}s^{-1}$; PAR0: μmol PAR $m^{-2}s^{-1}$; α_1, k_2: μmol CO_2 $m^{-2}s^{-1}{}^{\circ}C^{-1}$; α_2, k_3: μmol CO_2 $m^{-2}s^{-1}{}^{\circ}C^{-2}$; temperature and the temperature parameters are in °C. Parameters for shrub and grass are specifically optimized for this study, but other parameters are taken from Gourdji et al (2020).

	Evergreen Forest	Deciduous Forest	Mixed forest	Shrub	Savanna	Crop	Grass
T_{crit}	1	13	2	12	11	-1	3
T_{scale2}	0.05	0.1	0.05	0	0.2	0.05	0.2
T_{min}	0	0	0	0	0	2	2
T_{opt}	20	20	20	20	20	25	18
T_{max}	40	40	40	40	40	40	40
PAR_0	477.3	594	453	320	722	2782	900
λ	-0.122	-0.096	-0.121	-0.074	-0.10	-0.078	-0.124
β	0.560	-14.048	0.077	0.922	-4.124	-0.156	-1.650
α_1	0.120	1.766	0.132	-0.114	0.68	0.072	0.180
α_2	0.003	-0.048	0.001	0.002	-0.018	-0.001	-0.006
γ	1.430	5.349	3.20	5.944	3.269	5.501	9.050
k_1	-0.531	9.008	-0.799	0.570	2.698	0.145	0.944
k_2	0.181	-1.207	0.182	-0.109	-0.382	-0.152	-0.260
k_3	-0.005	0.038	-0.002	0.004	0.016	0.016	0.013

Table 2. configurations for nested-domain sensitivity simulations

Simulations	configuration	Purpose
Control	fully coupled	to diagnose the formation mechanism of the CO_2 band ahead of the cold front
clear-sky-photosynthesis	use clear-sky radiation to drive VPRM	The difference between clear-sky-photosynthesis and control runs shows the impact of clouds shading on terrestrial CO_2 fluxes, and subsequent impact on frontal CO_2 structures
clear-sky-surface-energy	use clear-sky radiation to drive the Noah land surface model	The difference between clear-sky-surface-energy and control runs shows the impact of clouds on surface energy balance, and subsequent impact on frontal CO_2 structures

Table 3. Overall statistics for simulated CO_2 over six NOAA towers during both daytime and nighttime by WRF-VPRM_G in this study and WRF-VPRM in Hu et al. (2020b).
The metrics include correlation coefficient *r*, mean bias (MB), mean absolute gross error (MAGE), root mean-square error (RMSE), and normalized mean bias (NMB). Their formula can be found in Seigneur et al. (2000).

	day and night											
Sites	AMT		BAO		LEF		SCT		WBI		WKT	
Simulations	VPRM_G	VPRM	VPRM_G	VPRM	VPRM_G	VPRM	VPRM_G	VPRM	VPRM_G	VPRM	VPRM_G	VPRM
Mean obs, ppm	415.12	415.12	417.12	417.12	411.33	411.33	416.47	416.47	416.19	416.19	414.32	414.32
Mean sim, ppm	410.84	406.16	414.72	412.66	410.05	405.63	417.67	414.42	415.42	409.39	415.59	410.72
Number	8153	8153	4742	4742	8124	8124	7940	7940	7754	7754	8024	8024
r	0.52	0.34	0.51	0.45	0.65	0.57	0.75	0.71	0.63	0.46	0.71	0.57
MB, ppm	-4.28	-8.96	-2.39	-4.45	-1.29	-5.70	1.20	-2.05	-0.77	-6.80	1.27	-3.61
MAGE, ppm	7.91	10.19	6.89	7.41	5.31	6.77	5.84	6.07	7.04	8.81	5.07	5.74
RMSE, ppm	15.54	19.00	10.84	11.80	9.05	11.52	8.03	8.74	11.58	15.48	7.01	8.84
NMB, %	-1.0	-2.2	-0.6	-1.1	-0.3	-1.4	0.3	-0.5	-0.2	-1.6	0.3	-0.9

Table 4. Evaluation statistics for simulated CO_2 over six NOAA towers during daytime between 10-18 CST.

	late day (10-18CST)											
Sites	AMT		BAO		LEF		SCT		WBI		WKT	
Simulations	VPRM_G	VPRM	VPRM_G	VPRM	VPRM_G	VPRM	VPRM_G	VPRM	VPRM_G	VPRM	VPRM_G	VPRM
Mean obs, ppm	405.57	405.57	412.52	412.52	405.62	405.62	407.39	407.39	408.43	408.43	408.25	408.25
Mean sim, ppm	406.5	403.43	410.96	410.3	407.36	403.98	410.57	408.4	411.04	406.81	410.95	408.44
Number	2836	2836	1642	1642	2826	2826	2771	2771	2676	2676	2782	2782
r	0.86	0.84	0.51	0.46	0.90	0.91	0.75	0.75	0.86	0.86	0.78	0.76
MB, ppm	0.92	-2.15	-1.56	-2.23	1.74	-1.64	3.19	1.02	2.61	-1.62	2.70	0.19
MAGE, ppm	3.98	4.28	5.62	5.88	3.68	3.48	4.86	4.13	5.32	4.85	4.14	3.28
RMSE, ppm	5.75	6.4	10.41	10.84	5.22	5.11	6.52	5.70	7.38	7.19	5.44	4.56
NMB, %	0.2	-0.5	-0.4	-0.5	0.4	-0.4	0.8	0.2	0.6	-0.4	0.7	0

Table 5. Evaluation statistics for simulated CO_2 over six NOAA towers during nighttime between 22-06 CST.

	late night (22-06CST)											
Sites	AMT		BAO		LEF		SCT		WBI		WKT	
Simulations	VPRM_G	VPRM	VPRM_G	VPRM	VPRM_G	VPRM	VPRM_G	VPRM	VPRM_G	VPRM	VPRM_G	VPRM
Mean obs, ppm	424.99	424.99	421.1	421.1	416.99	416.99	424.73	424.73	423.13	423.13	419.43	419.43
Mean sim, ppm	414.62	408.58	417.85	414.65	412.58	407.26	423.64	419.52	418.95	411.67	419.22	412.53
Number	3197	3197	1865	1865	3182	3182	3100	3100	3055	3055	3152	3152
r	0.21	-0.12	0.39	0.34	0.24	0.11	0.57	0.50	0.31	-0.02	0.53	0.32
MB, ppm	-10.38	-16.42	-3.25	-6.45	-4.41	-9.72	-1.08	-5.20	-4.19	-11.46	-0.21	-6.9
MAGE, ppm	12.69	16.88	7.93	8.81	7.10	10.16	6.52	7.82	8.86	12.50	5.75	8.06
RMSE, ppm	22.79	27.79	11.29	12.79	12.02	15.91	9.10	10.89	14.67	20.66	8.11	11.54
NMB, %	-2.4	-3.9	-0.8	-1.5	-1.1	-2.3	-0.3	-1.2	-1.	-2.7	0	-1.6

Figure captions:

Figure 1. (a) enhanced vegetation index (EVI) on 4 August 2016, and (b) dominant vegetation types including water, evergreen forest, deciduous forest, mixed forest, shrubland, savanna, cropland, grassland, and urban derived from MODIS data in the simulation domain. The second domain with a 4 km grid spacing over the Northern Great Plains is marked. Six NOAA tower sites (LEF [WI], AMT [ME], WBI [IA], SCT [SC], BAO [CO], and WKT [TX]) are marked with hollow diamonds. The ACT-America B200 flight track is also marked. (c) MODIS cloud image on this day overlaid with OCO-2 XCO_2 observation.

Figure 2. Evaluation of (a,b) hourly CO_2 flux and (c,d) its median diurnal variation during growing season simulated by (left) VPRM with respiration parametrization using eq. (2) (Mahadevan et al., 2008) and (right) VPRM_G using eq. (4) (Gourdji et al., 2020) comparing to the NEE measurements at US-Ne3, a crop site. Growing season mean bias (MB) of day and nighttime fluxes are marked in (a) and (b).

Figure 3. Near-surface CO_2 in 2016, observed at six NOAA tower sites and simulated by WRF-VPRM_G. Note that CO_2 is measured at different heights AGL at different towers, simulated values are extracted at the corresponding model height. Nighttime and daytime mean bias (MB) of CO_2 at each site is marked.

Figure 4. Median diurnal variation of near-surface CO_2 during growing season (June-September) in 2016, observed at six NOAA tower sites and simulated by WRF-VPRM_G. Note that CO_2 is measured at different heights AGL at different towers, simulated values are extracted at the corresponding model height.

Figure 5. Near-surface CO_2 in first half of July 2016 (growing season for most sites), observed at six NOAA tower sites and simulated by WRF-VPRM_G in this study and WRF-VPRM in Hu et al. (2020b). Nighttime is shaded.

Figure 6. Mean CO_2 profiles in growing season (June-September) of 2016 (1st row) observed at (left) LEF and (right) AMT NOAA towers and simulated by (2nd row) WRF-VPRM_G in this study and (3rd row) WRF-VPRM in Hu et al. (2020b).

Figure 7. same as Figure 5, but at (left) WBI and (right) SCT NOAA towers.

Figure 8. same as Figure 5, but at (left) BAO and (right) WKT NOAA towers.

Figure 9. (1st row) Profiles of CO_2, potential temperature (θ), and water vapor mixing ratio simulated at 1000 CST and observed during the C130 ascending time between 1000-1015 CST on August 4 over the Lincoln airport (40.8367°N, 96.7619°W), and profiles of (left to right) wind speed, θ, and water vapor mixing ratio at 0600 CST on August 4 simulated and observed at sounding sites: (2nd-4th rows) KLBF, KOAX, and KTOP, which are marked on Fig. 10.

Figure 10. (a,c) horizontal (at ~995m above sea level) and (b,d) vertical cross sections of (left) CO_2 and (right) equivalent potential temperature (θ_e) through the B200 flight track at 1200 CST on August 4 simulated by WRF-VPRM_G, overlaid with B200 aircraft CO_2 data. Note that the flight path and CO_2 data are marked in panel a. The CST time is marked along the flight path.

Figure 11. (a) vertical cross sections of total CO_2 through the B200 flight track at 1200 CST on August 4 simulated by WRF-VPRM_G in the nested inner domain, overlaid with B200 aircraft CO_2 data and (b-f) CO_2 components including background, biogenic, anthropogenic, respiration, and photosynthesis CO_2. Location of Lincoln is marked using a star on X-Axis.

Figure 12. (a) Total CO_2 through the B200 flight track at 1200 CST on August 4 in the nested inner domain simulated by WRF-VPRM_G and WRF-VPRM, along with B200 aircraft CO_2 data in the boundary layer during 11:20-13:10 CST and (b-f) simulated CO_2 components including background, biogenic, anthropogenic, respiration, and photosynthesis CO_2. Location of Lincoln is marked using a star on X-Axis.

Figure 13. (top to bottom) Surface biogenic CO_2, respiration, and photosynthesis CO_2 at (a,b,c) 08 and (d,e,f) 12 CST. B200 aircraft CO_2 data in the boundary layer is overlaid for location reference.

Figure 14. (a) vertical cross sections of total CO_2 through the B200 flight track at 0200 CST on August 4 simulated by WRF-VPRM_G in the nested inner domain, overlaid with B200 aircraft CO_2 data and (b-d) CO_2 components including background, biogenic, anthropogenic CO_2, (e-f) vertical velocity, and hydrometer mixing ratio.

Figure 15. (top to bottom) surface short wave radiation, GEE, and biogenic CO_2 simulated by (left) control and (middle) the clear-sky-photosynthesis sensitivity simulation, and (right) their difference at 10 CST. B200 aircraft CO_2 data in the boundary layer at ~12 CST is overlaid.

Figure 16. difference of (top to bottom) surface short wave radiation, GEE, and biogenic CO_2 simulated by the control and the clear-sky-photosynthesis sensitivity simulation, at (left) 11 CST and (right) 12 CST. B200 aircraft CO_2 data in the boundary layer at ~12 CST is overlaid.

Figure 17. same as Figure 12, but simulated by the Sensitivity1 (clear-sky-photosynthesis) and Sensitivity2 (clear-sky-surface-energy) simulations.

Figure 18. (top to bottom) temperature at 2 m AGL (T2), NEE, and biogenic CO_2 simulated by (left) control and (middle) the clear-sky-surface-energy sensitivity simulation, and (right) their difference at 10 CST. B200 aircraft CO_2 data in the boundary layer at ~12 CST is overlaid.

References:

Ai, J., Xiao, S., Feng, H., Wang, H., Jia, G., & Hu, Y. (2020). A global terrestrial ecosystem respiration dataset (2001-2010) estimated with MODIS land surface temperature and vegetation indices. *Big Earth Data, 4*(2), 142-152. 10.1080/20964471.2020.1768001

Aubinet, M. (2008). EDDY COVARIANCE CO2 FLUX MEASUREMENTS IN NOCTURNAL CONDITIONS: AN ANALYSIS OF THE PROBLEM. *Ecological Applications, 18*(6), 1368-1378. https://doi.org/10.1890/06-1336.1

Bakwin, P. S., Tans, P. P., Hurst, D. F., & Zhao, C. (1998). Measurements of carbon dioxide on very tall towers: results of the NOAA/CMDL program. *Tellus B: Chemical and Physical Meteorology, 50*(5), 401-415. 10.3402/tellusb.v50i5.16216

Ballav, S., Patra, P. K., Sawa, Y., Matsueda, H., Adachi, A., Onogi, S., . . . De, U. K. (2016). Simulation of CO2concentrations at Tsukuba tall tower using WRF-CO2tracer transport model. *Journal of Earth System Science, 125*(1), 47-64. 10.1007/s12040-015-0653-y

Barth, M. C., Kim, S. W., Wang, C., Pickering, K. E., Ott, L. E., Stenchikov, G., . . . Telenta, B. (2007). Cloud-scale model intercomparison of chemical constituent transport in deep convection. *Atmos. Chem. Phys., 7*(18), 4709-4731. 10.5194/acp-7-4709-2007

Bell, E., O'Dell, C. W., Davis, K. J., Campbell, J., Browell, E., Scott Denning, A., . . . Weir, B. (2020). Evaluation of OCO-2 X Variability at Local and Synoptic Scales using Lidar and In Situ Observations from the ACT-America Campaigns. *Journal of Geophysical Research: Atmospheres, 125*(10), e2019JD031400. 10.1029/2019jd031400

Brioude, J., Angevine, W. M., Ahmadov, R., Kim, S. W., Evan, S., McKeen, S. A., . . . Trainer, M. (2013). Top-down estimate of surface flux in the Los Angeles Basin using a mesoscale inverse modeling technique: assessing anthropogenic emissions of CO, NOx and CO2 and their impacts. *Atmospheric Chemistry and Physics, 13*(7), 3661-3677. 10.5194/acp-13-3661-2013

Brioude, J., Petron, G., Frost, G. J., Ahmadov, R., Angevine, W. M., Hsie, E. Y., . . . Gurney, K. R. (2012). A new inversion method to calculate emission inventories without a prior at mesoscale: Application to the anthropogenic CO2 emission from Houston, Texas. *Journal of Geophysical Research-Atmospheres, 117*. D05312, 10.1029/2011jd016918

Buchmann, N. (2000). Biotic and abiotic factors controlling soil respiration rates in Picea abies stands. *Soil Biology and Biochemistry, 32*(11), 1625-1635. https://doi.org/10.1016/S0038-0717(00)00077-8

Chan, D., YUEN, C. W., HIGUCHI, K., SHASHKOV, A., LIU, J., CHEN, J., & WORTHY, D. (2004). On the CO2 exchange between the atmosphere and the biosphere: the role of synoptic and mesoscale processes. *Tellus Series B-Chemical and Physical Meteorology, 56*(3), 194-212. 10.1111/j.1600-0889.2004.00104.x

Chen, F., & Dudhia, J. (2001). Coupling an advanced land surface-hydrology model with the Penn State-NCAR MM5 modeling system. Part I: Model implementation and sensitivity. *Monthly Weather Review, 129*(4), 569-585. Doi 10.1175/1520-0493(2001)129<0569:Caalsh>2.0.Co;2

Crevoisier, C., Sweeney, C., Gloor, M., Sarmiento, J. L., & Tans, P. P. (2010). Regional US carbon sinks from three-dimensional atmospheric CO₂ sampling. *Proceedings of the National Academy of Sciences, 107*(43), 18348-18353. 10.1073/pnas.0900062107

719 Davidson, E. A., Belk, E., & Boone, R. D. (1998). Soil water content and temperature as
720 independent or confounded factors controlling soil respiration in a temperate mixed
721 hardwood forest. *Global Change Biology, 4*(2), 217-227. 10.1046/j.1365-
722 2486.1998.00128.x
723 Davis, K. J., Bakwin, P. S., Yi, C., Berger, B. W., Zhao, C., Teclaw, R. M., & Isebrands, J. G.
724 (2003). The annual cycles of CO2 and H2O exchange over a northern mixed forest as
725 observed from a very tall tower. *Global Change Biology, 9*(9), 1278-1293.
726 doi:10.1046/j.1365-2486.2003.00672.x
727 Davis, K. J., Obland, M. D., Lin, B., Lauvaux, T., O'Dell, C., Meadows, B., . . . Pauly, R. M.
728 (2018). ACT-America: L3 Merged In Situ Atmospheric Trace Gases and Flask Data,
729 Eastern USA: ORNL Distributed Active Archive Center,
730 https://doi.org/10.3334/ORNLDAAC/1593.
731 Dayalu, A., Munger, J. W., Wofsy, S. C., Wang, Y., Nehrkorn, T., Zhao, Y., . . . Luus, K. (2018).
732 Assessing biotic contributions to CO2 fluxes in northern China using the Vegetation,
733 Photosynthesis and Respiration Model (VPRM-CHINA) and observations from 2005 to
734 2009. *Biogeosciences, 15*(21), 6713-6729. 10.5194/bg-15-6713-2018
735 Diaz-Isaac, L. I., Lauvaux, T., & Davis, K. J. (2018). Impact of physical parameterizations and
736 initial conditions on simulated atmospheric transport and CO2 mole fractions in the US
737 Midwest. *Atmospheric Chemistry and Physics, 18*(20), 14813-14835. 10.5194/acp-18-
738 14813-2018
739 Digangi, J. P., Choi, Y., Nowak, J. B., Halliday, H. S., & Yang, M. M. (2018). *ACT-America: L2
740 In Situ Atmospheric CO2, CO, CH4, and O3 Concentrations, Eastern USA*. Retrieved
741 from: https://daac.ornl.gov/cgi-bin/dsviewer.pl?ds_id=1556
742 Dong, J. W., Xiao, X. M., Wagle, P., Zhang, G. L., Zhou, Y. T., Jin, C., . . . Moore, B. (2015).
743 Comparison of four EVI-based models for estimating gross primary production of maize
744 and soybean croplands and tallgrass prairie under severe drought. *Remote Sensing of
745 Environment, 162*, 154-168. 10.1016/j.rse.2015.02.022
746 Dudhia, J. (1989). Numerical Study of Convection Observed during the Winter Monsoon
747 Experiment Using a Mesoscale Two-Dimensional Model. *Journal of the Atmospheric
748 Sciences, 46*(20), 3077-3107. Doi 10.1175/1520-0469(1989)046<3077:Nsocod>2.0.Co;2
749 Fang, C., & Moncrieff, J. B. (2001). The dependence of soil CO2 efflux on temperature. *Soil
750 Biology and Biochemistry, 33*(2), 155-165. https://doi.org/10.1016/S0038-
751 0717(00)00125-5
752 Gomez, B., & Miguez-Macho, G. (2017). The impact of wave number selection and spin-up time
753 in spectral nudging. *Quarterly Journal of the Royal Meteorological Society, 143*(705),
754 1772-1786. 10.1002/qj.3032
755 Gourdji, S. M., Lopez-Coto, I., Karion, A., Mueller, K., Ghosh, S., Baker, I., . . . Zhou, Y.
756 (2020). *Modeling (and evaluating) the upwind biosphere for urban CO2 inversions in the
757 Northeast Corridor.* Paper presented at the ACT-America Community Workshop,
758 https://drive.google.com/drive/folders/1hm0e0QuIp3g4TAQ8KWejSfc7VW9ZXoUA.
759 Grell, G. A., & Devenyi, D. (2002). A generalized approach to parameterizing convection
760 combining ensemble and data assimilation techniques. *Geophysical Research Letters,
761 29*(14). 1693, 10.1029/2002gl015311
762 Guan, D.-X., Wu, J.-B., Zhao, X.-S., Han, S.-J., Yu, G.-R., Sun, X.-M., & Jin, C.-J. (2006). CO2
763 fluxes over an old, temperate mixed forest in northeastern China. *Agricultural and Forest
764 Meteorology, 137*(3), 138-149. https://doi.org/10.1016/j.agrformet.2006.02.003

765 Haynes, K. D., Baker, I. T., Denning, A. S., Stöckli, R., Schaefer, K., Lokupitiya, E. Y., &
766 Haynes, J. M. (2019). Representing Grasslands Using Dynamic Prognostic Phenology
767 Based on Biological Growth Stages: 1. Implementation in the Simple Biosphere Model
768 (SiB4). *Journal of Advances in Modeling Earth Systems, 11*(12), 4423-4439.
769 10.1029/2018ms001540
770 Hilton, T. W., Davis, K. J., Keller, K., & Urban, N. M. (2016). *NACP VPRM NEE Parameters*
771 *Optimized to North American Flux Tower Sites, 2000-2006*. Retrieved from:
772 http://daac.ornl.gov/cgi-bin/dsviewer.pl?ds_id=1349
773 Hong, S. Y., Noh, Y., & Dudhia, J. (2006). A new vertical diffusion package with an explicit
774 treatment of entrainment processes. *Monthly Weather Review, 134*(9), 2318-2341. Doi
775 10.1175/Mwr3199.1
776 Houghton, J. T., & Moir, D. W. (1977). *The Physics of Atmospheres*: Cambridge University
777 Press.
778 Hu, X.-M., Crowell, S., Wang, Q., Feng, S., & Davis, K. (2020a). *Examine CO2 bands along*
779 *cold fronts observed during ACT-America using WRF-VPRM.* Paper presented at the
780 ACT-America Community Workshop,
781 https://drive.google.com/drive/folders/1hm0e0QuIp3g4TAQ8KWejSfc7VW9ZXoUA.
782 Hu, X.-M., Doughty, D. C., Sanchez, K. J., Joseph, E., & Fuentes, J. D. (2012). Ozone variability
783 in the atmospheric boundary layer in Maryland and its implications for vertical transport
784 model. *Atmospheric Environment, 46*, 354-364. DOI 10.1016/j.atmosenv.2011.09.054
785 Hu, X.-M., Fuentes, J. D., & Zhang, F. (2010a). Downward transport and modification of
786 tropospheric ozone through moist convection. *Journal of Atmospheric Chemistry, 65*(1),
787 13-35. 10.1007/s10874-010-9179-5
788 Hu, X.-M., Klein, P. M., & Xue, M. (2013). Evaluation of the updated YSU planetary boundary
789 layer scheme within WRF for wind resource and air quality assessments. *Journal of*
790 *Geophysical Research-Atmospheres, 118*(18), 10490-10505. 10.1002/jgrd.50823
791 Hu, X.-M., Nielsen-Gammon, J. W., & Zhang, F. Q. (2010b). Evaluation of Three Planetary
792 Boundary Layer Schemes in the WRF Model. *Journal of Applied Meteorology and*
793 *Climatology, 49*(9), 1831-1844. 10.1175/2010jamc2432.1
794 Hu, X.-M., Xue, M., Kong, F., & Zhang, H. (2019a). Meteorological Conditions During an
795 Ozone Episode in Dallas-Fort Worth, Texas, and Impact of Their Modeling Uncertainties
796 on Air Quality Prediction. *Journal of Geophysical Research: Atmospheres, 124*(4), 1941-
797 1961. 10.1029/2018jd029791
798 Hu, X.-M., Xue, M., & Li, X. (2019b). The Use of High-Resolution Sounding Data to Evaluate
799 and Optimize Nonlocal PBL Schemes for Simulating the Slightly Stable Upper
800 Convective Boundary Layer. *Monthly Weather Review, 147*(10), 3825-3841.
801 10.1175/mwr-d-19-0085.1
802 Hu, X. M., Crowell, S., Wang, Q., Zhang, Y., Davis, K. J., Xue, M., . . . DiGangi, J. P. (2020b).
803 Dynamical Downscaling of CO2 in 2016 Over the Contiguous United States Using WRF-
804 VPRM, a Weather-Biosphere-Online-Coupled Model. *Journal of Advances in Modeling*
805 *Earth Systems, 12*(4), e2019MS001875. 10.1029/2019ms001875
806 Hu, X. M., Xue, M., & McPherson, R. A. (2017). The Importance of Soil-Type Contrast in
807 Modulating August Precipitation Distribution Near the Edwards Plateau and Balcones
808 Escarpment in Texas. *Journal of Geophysical Research-Atmospheres, 122*(20), 10711-
809 10728. 10.1002/2017jd027035

Hu, X. M., Xue, M., McPherson, R. A., Martin, E., Rosendahl, D. H., & Qiao, L. (2018). Precipitation Dynamical Downscaling Over the Great Plains. *Journal of Advances in Modeling Earth Systems, 10*(2), 421-447. 10.1002/2017ms001154

Hurwitz, M. D., Ricciuto, D. M., Bakwin, P. S., Davis, K. J., Wang, W., Yi, C., & Butler, M. P. (2004). Transport of Carbon Dioxide in the Presence of Storm Systems over a Northern Wisconsin Forest. *Journal of the Atmospheric Sciences, 61*(5), 607-618. 10.1175/1520-0469(2004)061<0607:Tocdit>2.0.Co;2

Jiang, J. H., Livesey, N. J., Su, H., Neary, L., McConnell, J. C., & Richards, N. A. D. (2007). Connecting surface emissions, convective uplifting, and long-range transport of carbon monoxide in the upper troposphere: New observations from the Aura Microwave Limb Sounder. *Geophysical Research Letters, 34*(18). 10.1029/2007gl030638

Kanamitsu, M., Ebisuzaki, W., Woollen, J., Yang, S. K., Hnilo, J. J., Fiorino, M., & Potter, G. L. (2002). NCEP-DOE AMIP-II reanalysis (R-2). *Bulletin of the American Meteorological Society, 83*(11), 1631-1643. 10.1175/Bams-83-11-1631

Konovalov, I. B., Berezin, E. V., Ciais, P., Broquet, G., Beekmann, M., Hadji-Lazaro, J., . . . Schulze, E. D. (2014). Constraining CO₂ emissions from open biomass burning by satellite observations of co-emitted species: a method and its application to wildfires in Siberia. *Atmos. Chem. Phys., 14*(19), 10383-10410. 10.5194/acp-14-10383-2014

Langford, A. O., Tucker, S. C., Senff, C. J., Banta, R. M., Brewer, W. A., Alvarez II, R. J., . . . Williams, E. J. (2010). Convective venting and surface ozone in Houston during TexAQS 2006. *Journal of Geophysical Research: Atmospheres, 115*(D16). 10.1029/2009jd013301

Lee, T. R., De Wekker, S. F. J., Andrews, A. E., Kofler, J., & Williams, J. (2012). Carbon dioxide variability during cold front passages and fair weather days at a forested mountaintop site. *Atmospheric Environment, 46*, 405-416. https://doi.org/10.1016/j.atmosenv.2011.09.068

Li, X., Hu, X.-M., Cai, C., Jia, Q., Zhang, Y., Liu, J., . . . Crowell, S. M. R. (2020). Terrestrial CO2 Fluxes, Concentrations, Sources and Budget in Northeast China: Observational and Modeling Studies. *Journal of Geophysical Research: Atmospheres*, e2019JD031686. 10.1029/2019jd031686

Lindenmaier, R., Dubey, M. K., Henderson, B. G., Butterfield, Z. T., Herman, J. R., Rahn, T., & Lee, S. H. (2014). Multiscale observations of CO2, (CO2)-C-13, and pollutants at Four Corners for emission verification and attribution. *Proceedings of the National Academy of Sciences of the United States of America, 111*(23), 8386-8391. 10.1073/pnas.1321883111

Lloyd, J., & Taylor, J. A. (1994). On the Temperature Dependence of Soil Respiration. *Functional Ecology, 8*(3), 315-323. 10.2307/2389824

Lopez-Coto, I., Prasad, K., & Whetstone, J. R. (2017). *Carbon Dioxide Biogenic vs Anthropogenic Sectoral Contribution for the Indianapolis Flux Experiment (INFLUX)*. Retrieved from Gaithersburg, MD: http://dx.doi.org/10.6028/nist.sp.1237

Loranty, M. M., Goetz, S. J., Rastetter, E. B., Rocha, A. V., Shaver, G. R., Humphreys, E. R., & Lafleur, P. M. (2011). Scaling an Instantaneous Model of Tundra NEE to the Arctic Landscape. *Ecosystems, 14*(1), 76-93. 10.1007/s10021-010-9396-4

Mahadevan, P., Wofsy, S. C., Matross, D. M., Xiao, X. M., Dunn, A. L., Lin, J. C., . . . Gottlieb, E. W. (2008). A satellite-based biosphere parameterization for net ecosystem CO2

exchange: Vegetation Photosynthesis and Respiration Model (VPRM). *Global Biogeochemical Cycles, 22*(2). Gb2005, 10.1029/2006gb002735

Matross, D. M., Andrews, A., Pathmathevan, M., Gerbig, C., Lin, J. C., Wofsy, S. C., . . . Hollinger, D. Y. (2006). Estimating regional carbon exchange in New England and Quebec by combining atmospheric, ground-based and satellite data. *Tellus B: Chemical and Physical Meteorology, 58*(5), 344-358. 10.1111/j.1600-0889.2006.00206.x

Mlawer, E. J., Taubman, S. J., Brown, P. D., Iacono, M. J., & Clough, S. A. (1997). Radiative transfer for inhomogeneous atmospheres: RRTM, a validated correlated-k model for the longwave. *Journal of Geophysical Research-Atmospheres, 102*(D14), 16663-16682. Doi 10.1029/97jd00237

Morrison, H., Thompson, G., & Tatarskii, V. (2009). Impact of Cloud Microphysics on the Development of Trailing Stratiform Precipitation in a Simulated Squall Line: Comparison of One- and Two-Moment Schemes. *Monthly Weather Review, 137*(3), 991-1007. 10.1175/2008mwr2556.1

Murayama, S., Saigusa, N., Chan, D., Yamamoto, S., Kondo, H., & Eguchi, Y. (2003). Temporal variations of atmospheric CO2 concentration in a temperate deciduous forest in central Japan. *Tellus B: Chemical and Physical Meteorology, 55*(2), 232-243. 10.3402/tellusb.v55i2.16751

O'Dell, C. W., Eldering, A., Wennberg, P. O., Crisp, D., Gunson, M. R., Fisher, B., . . . Velazco, V. A. (2018). Improved retrievals of carbon dioxide from Orbiting Carbon Observatory-2 with the version 8 ACOS algorithm. *Atmospheric Measurement Techniques, 11*(12), 6539-6576. 10.5194/amt-11-6539-2018

Oda, T., Maksyutov, S., & Andres, R. J. (2018). The Open-source Data Inventory for Anthropogenic CO2, version 2016 (ODIAC2016): a global monthly fossil fuel CO2 gridded emissions data product for tracer transport simulations and surface flux inversions. *Earth Syst. Sci. Data, 10*(1), 87-107. 10.5194/essd-10-87-2018

Otte, T. L., Nolte, C. G., Otte, M. J., & Bowden, J. H. (2012). Does Nudging Squelch the Extremes in Regional Climate Modeling? *Journal of Climate, 25*(20), 7046-7066. 10.1175/Jcli-D-12-00048.1

Pal, S., Davis, K. J., Lauvaux, T., Browell, E. V., Gaudet, B. J., Stauffer, D. R., . . . Zhang, F. (2020). Observations of Greenhouse Gas Changes Across Summer Frontal Boundaries in the Eastern United States. *Journal of Geophysical Research: Atmospheres, 125*(5), e2019JD030526. 10.1029/2019jd030526

Parazoo, N. C., Denning, A. S., Kawa, S. R., Corbin, K. D., Lokupitiya, R. S., & Baker, I. T. (2008). Mechanisms for synoptic variations of atmospheric CO₂ in North America, South America and Europe. *Atmos. Chem. Phys., 8*(23), 7239-7254. 10.5194/acp-8-7239-2008

Park, C., Park, S.-Y., Gurney, K. R., Gerbig, C., DiGangi, J. P., Choi, Y., & Lee, H. W. (2020). Numerical simulation of atmospheric CO2 concentration and flux over the Korean Peninsula using WRF-VPRM model during Korus-AQ 2016 campaign. *Plos One, 15*(1), e0228106. 10.1371/journal.pone.0228106

Peters, W., Jacobson, A. R., Sweeney, C., Andrews, A. E., Conway, T. J., Masarie, K., . . . Tans, P. P. (2007). An atmospheric perspective on North American carbon dioxide exchange: CarbonTracker. *Proceedings of the National Academy of Sciences of the United States of America, 104*(48), 18925-18930. 10.1073/pnas.0708986104

Raich, J. W., Potter, C. S., & Bhagawati, D. (2002). Interannual variability in global soil respiration, 1980–94. *Global Change Biology, 8*(8), 800-812. 10.1046/j.1365-2486.2002.00511.x

Reuter, M., Buchwitz, M., Schneising, O., Krautwurst, S., O'Dell, C. W., Richter, A., . . . Burrows, J. P. (2019). Towards monitoring localized CO2 emissions from space: co-located regional CO2 and NO2 enhancements observed by the OCO-2 and S5P satellites. *Atmos. Chem. Phys., 19*(14), 9371-9383. 10.5194/acp-19-9371-2019

Rey, A., Pegoraro, E., Tedeschi, V., De Parri, I., Jarvis, P. G., & Valentini, R. (2002). Annual variation in soil respiration and its components in a coppice oak forest in Central Italy. *Global Change Biology, 8*(9), 851-866. 10.1046/j.1365-2486.2002.00521.x

Schubert, P., Eklundh, L., Lund, M., & Nilsson, M. (2010). Estimating northern peatland CO2 exchange from MODIS time series data. *Remote Sensing of Environment, 114*(6), 1178-1189. https://doi.org/10.1016/j.rse.2010.01.005

Seigneur, C., Pun, B., Pai, P., Louis, J. F., Solomon, P., Emery, C., . . . Tombach, I. (2000). Guidance for the performance evaluation of three-dimensional air quality modeling systems for particulate matter and visibility. *Journal of the Air & Waste Management Association, 50*(4), 588-599.

Skamarock, W. C., Klemp, J., Dudhia, J., Gill, D., Barker, M., Duda, K., . . . Powers, J. (2008). *A description of the advanced research WRF version 3. NCAR Tech. Note TN-475_STR*.

Skamarock, W. C., & Klemp, J. B. (2008). A time-split nonhydrostatic atmospheric model for weather research and forecasting applications. *Journal of Computational Physics, 227*(7), 3465-3485. http://dx.doi.org/10.1016/j.jcp.2007.01.037

Sweeney, C., Karion, A., Wolter, S., Newberger, T., Guenther, D., Higgs, J. A., . . . Tans, P. P. (2015). Seasonal climatology of CO2 across North America from aircraft measurements in the NOAA/ESRL Global Greenhouse Gas Reference Network. *Journal of Geophysical Research: Atmospheres, 120*(10), 5155-5190. doi:10.1002/2014JD022591

Takahashi, T., Sutherland, S. C., Wanninkhof, R., Sweeney, C., Feely, R. A., Chipman, D. W., . . . de Baar, H. J. W. (2009). Climatological mean and decadal change in surface ocean pCO(2), and net sea-air CO2 flux over the global oceans. *Deep-Sea Research Part Ii-Topical Studies in Oceanography, 56*(8-10), 554-577.

Tang, J., Bolstad, P. V., Desai, A. R., Martin, J. G., Cook, B. D., Davis, K. J., & Carey, E. V. (2008). Ecosystem respiration and its components in an old-growth forest in the Great Lakes region of the United States. *Agricultural and Forest Meteorology, 148*(2), 171-185. https://doi.org/10.1016/j.agrformet.2007.08.008

Turnbull, J. C., Karion, A., Fischer, M. L., Faloona, I., Guilderson, T., Lehman, S. J., . . . Tans, P. P. (2011). Assessment of fossil fuel carbon dioxide and other anthropogenic trace gas emissions from airborne measurements over Sacramento, California in spring 2009. *Atmos. Chem. Phys., 11*(2), 705-721. 10.5194/acp-11-705-2011

Vincent, C. L., & Hahmann, A. N. (2015). The Impact of Grid and Spectral Nudging on the Variance of the Near-Surface Wind Speed. *Journal of Applied Meteorology and Climatology, 54*(5), 1021-1038. 10.1175/Jamc-D-14-0047.1

Wagle, P., Xiao, X. M., Torn, M. S., Cook, D. R., Matamala, R., Fischer, M. L., . . . Biradar, C. (2014). Sensitivity of vegetation indices and gross primary production of tallgrass prairie to severe drought. *Remote Sensing of Environment, 152*, 1-14. Doi 10.1016/J.Rse.2014.05.010

945 Wang, Q., Crowell, S., Hu, X.-M., & Davis, K. (2020). *Evaluation of Online and Offline*
946 *Regional Modeled CO2 Transport with INFLUX Observations.* Paper presented at the the
947 100th AMS Annual Meeting, Boston,
948 https://ams.confex.com/ams/2020Annual/meetingapp.cgi/Paper/364572.
949 Wang, W. G., Shen, X. Y., & Huang, W. Y. (2016). A Comparison of Boundary-Layer
950 Characteristics Simulated Using Different Parametrization Schemes. *Boundary-Layer*
951 *Meteorology, 161*(2), 375-403. 10.1007/s10546-016-0175-4
952 Wunch, D., Wennberg, P. O., Toon, G. C., Keppel-Aleks, G., & Yavin, Y. G. (2009). Emissions
953 of greenhouse gases from a North American megacity. *Geophysical Research Letters, 36*.
954 L15810, 10.1029/2009gl039825
955 Xiao, X. M., Hollinger, D., Aber, J., Goltz, M., Davidson, E. A., Zhang, Q. Y., & Moore, B.
956 (2004). Satellite-based modeling of gross primary production in an evergreen needleleaf
957 forest. *Remote Sensing of Environment, 89*(4), 519-534. 10.1016/j.rse.2003.11.008
958 Yang, S., Duan, F., Ma, Y., He, K., Zhu, L., Ma, T., . . . Kimoto, T. (2019a). Haze formation
959 indicator based on observation of critical carbonaceous species in the atmosphere.
960 *Environmental Pollution, 244*, 84-92. https://doi.org/10.1016/j.envpol.2018.10.006
961 Yang, Y., Hu, X.-M., Gao, S., & Wang, Y. (2019b). Sensitivity of WRF simulations with the
962 YSU PBL scheme to the lowest model level height for a sea fog event over the Yellow
963 Sea. *Atmospheric Research, 215*, 253-267.
964 https://doi.org/10.1016/j.atmosres.2018.09.004
965 Yi, C., Davis, K. J., Bakwin, P. S., Denning, A. S., Zhang, N., Desai, A., . . . Gerbig, C. (2004).
966 Observed covariance between ecosystem carbon exchange and atmospheric boundary
967 layer dynamics at a site in northern Wisconsin. *Journal of Geophysical Research:*
968 *Atmospheres, 109*(D8). 10.1029/2003jd004164
969 Yi, C., Davis, K. J., Berger, B. W., & Bakwin, P. S. (2001). Long-Term Observations of the
970 Dynamics of the Continental Planetary Boundary Layer. *Journal of the Atmospheric*
971 *Sciences, 58*(10), 1288-1299. 10.1175/1520-0469(2001)058<1288:Ltootd>2.0.Co;2
972 Zhang, Y., Xiao, X., Guanter, L., Zhou, S., Ciais, P., Joiner, J., . . . Stocker, B. D. (2016a).
973 Precipitation and carbon-water coupling jointly control the interannual variability of
974 global land gross primary production. *Scientific Reports, 6*, 39748. 10.1038/srep39748
975 Zhang, Y., Xiao, X. M., Jin, C., Dong, J. W., Zhou, S., Wagle, P., . . . Moore, B. (2016b).
976 Consistency between sun-induced chlorophyll fluorescence and gross primary production
977 of vegetation in North America. *Remote Sensing of Environment, 183*, 154-169.
978 10.1016/j.rse.2016.05.015
979 Zhang, Y., Xiao, X. M., Wolf, S., Wu, J., Wu, X. C., Gioli, B., . . . Ardo, J. (2018). Spatio-
980 Temporal Convergence of Maximum Daily Light-Use Efficiency Based on Radiation
981 Absorption by Canopy Chlorophyll. *Geophysical Research Letters, 45*(8), 3508-3519.
982 10.1029/2017gl076354
983 Zhang, Y., Xiao, X. M., Wu, X. C., Zhou, S., Zhang, G. L., Qin, Y. W., & Dong, J. W. (2017).
984 Data Descriptor: A global moderate resolution dataset of gross primary production of
985 vegetation for 2000-2016. *Scientific Data, 4*. 170165, 10.1038/sdata.2017.165
986 Zhou, Y., Williams, C. A., Lauvaux, T., Davis, K. J., Feng, S., Baker, I., . . . Wei, Y. (2020). A
987 Multiyear Gridded Data Ensemble of Surface Biogenic Carbon Fluxes for North
988 America: Evaluation and Analysis of Results. *Journal of Geophysical Research:*
989 *Biogeosciences, 125*(2), e2019JG005314. 10.1029/2019jg005314
990

Figures.

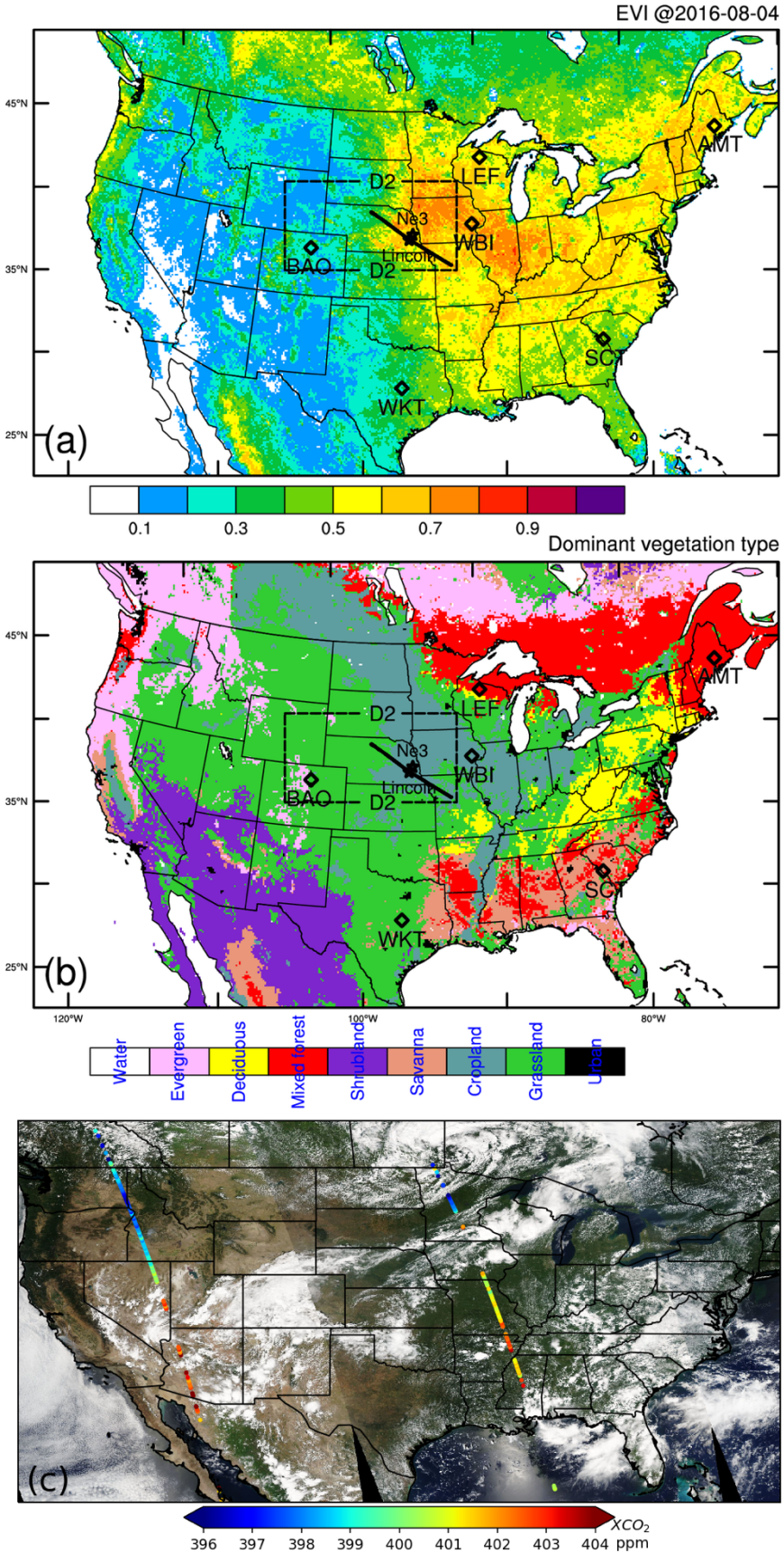
EVI @2016-08-04
45°N
35°N
25°N
(a)
D2
LEF
Ne3
WBI
Lincoln
BAO
D2
AMT
SCT
WKT
0.1
0.3
0.5
0.7
0.9
Dominant vegetation type
45°N
35°N
25°N
120°W
100°W
80°W
(b)
D2
LEF
Ne3
WBI
Lincoln
BAO
D2
AMT
SCT
WKT
Water
Evergreen
Deciduous
Mixed forest
Shrublands
Savanna
Cropland
Grassland
Urban
(c)
396
397
398
399
400
401
402
403
404
XCO_2 ppm

Figure 1. (a) enhanced vegetation index (EVI) on 4 August 2016, and (b) dominant vegetation types including water, evergreen forest, deciduous forest, mixed forest, shrubland, savanna, cropland, grassland, and urban derived from MODIS data in the simulation domain. The second domain with a 4 km grid spacing over the Northern Great Plains is marked. Six NOAA tower sites (LEF [WI], AMT [ME], WBI [IA], SCT [SC], BAO [CO], and WKT [TX]) are marked with hollow diamonds. The ACT-America B200 flight track is also marked. (c) MODIS cloud image on this day overlaid with OCO-2 XCO_2 observation.

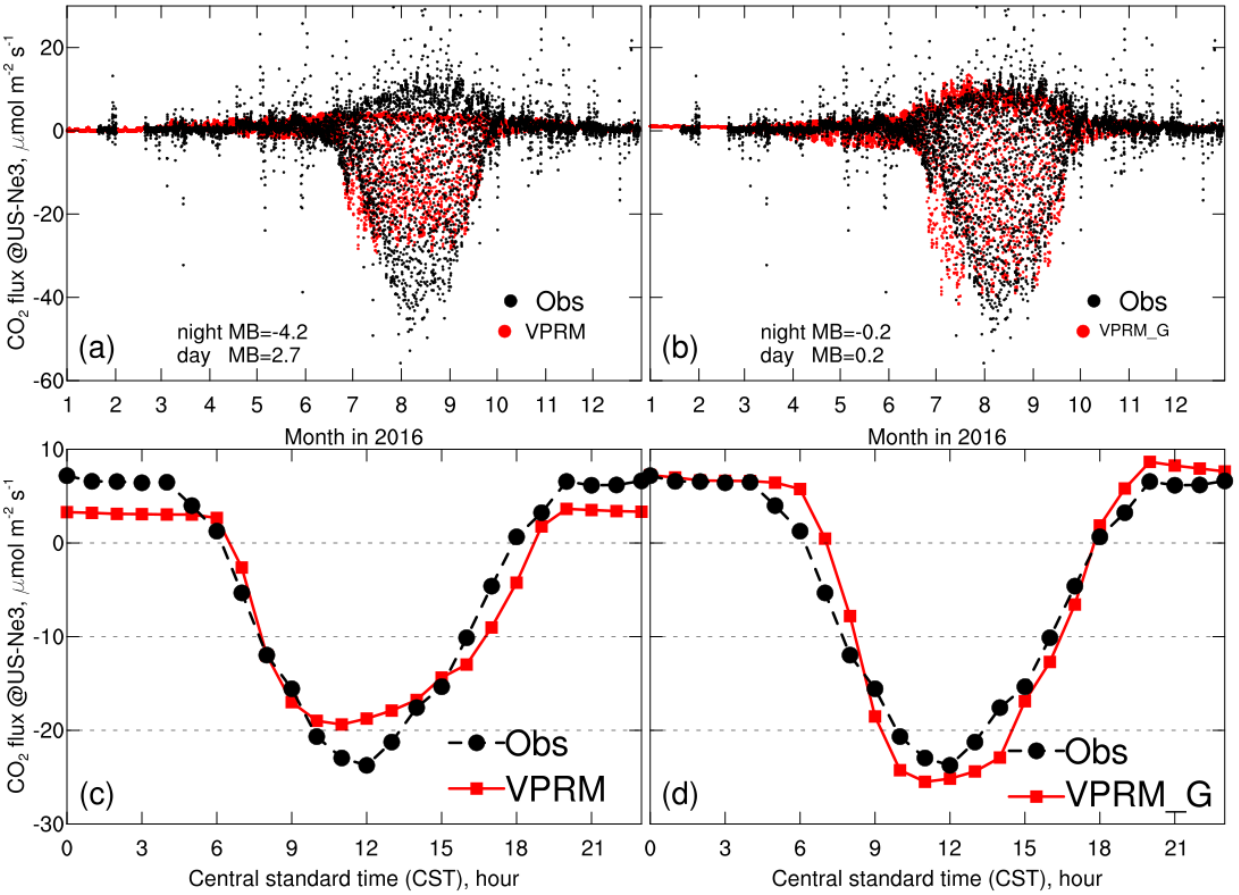

Figure 2. Evaluation of (a,b) hourly CO_2 flux and (c,d) its median diurnal variation during growing season simulated by (left) VPRM with respiration parametrization using eq. (2) (Mahadevan et al., 2008) and (right) VPRM_G using eq. (4) (Gourdji et al., 2020) comparing to the NEE measurements at US-Ne3, a crop site. Growing season mean bias (MB) of day and nighttime fluxes are marked in (a) and (b).

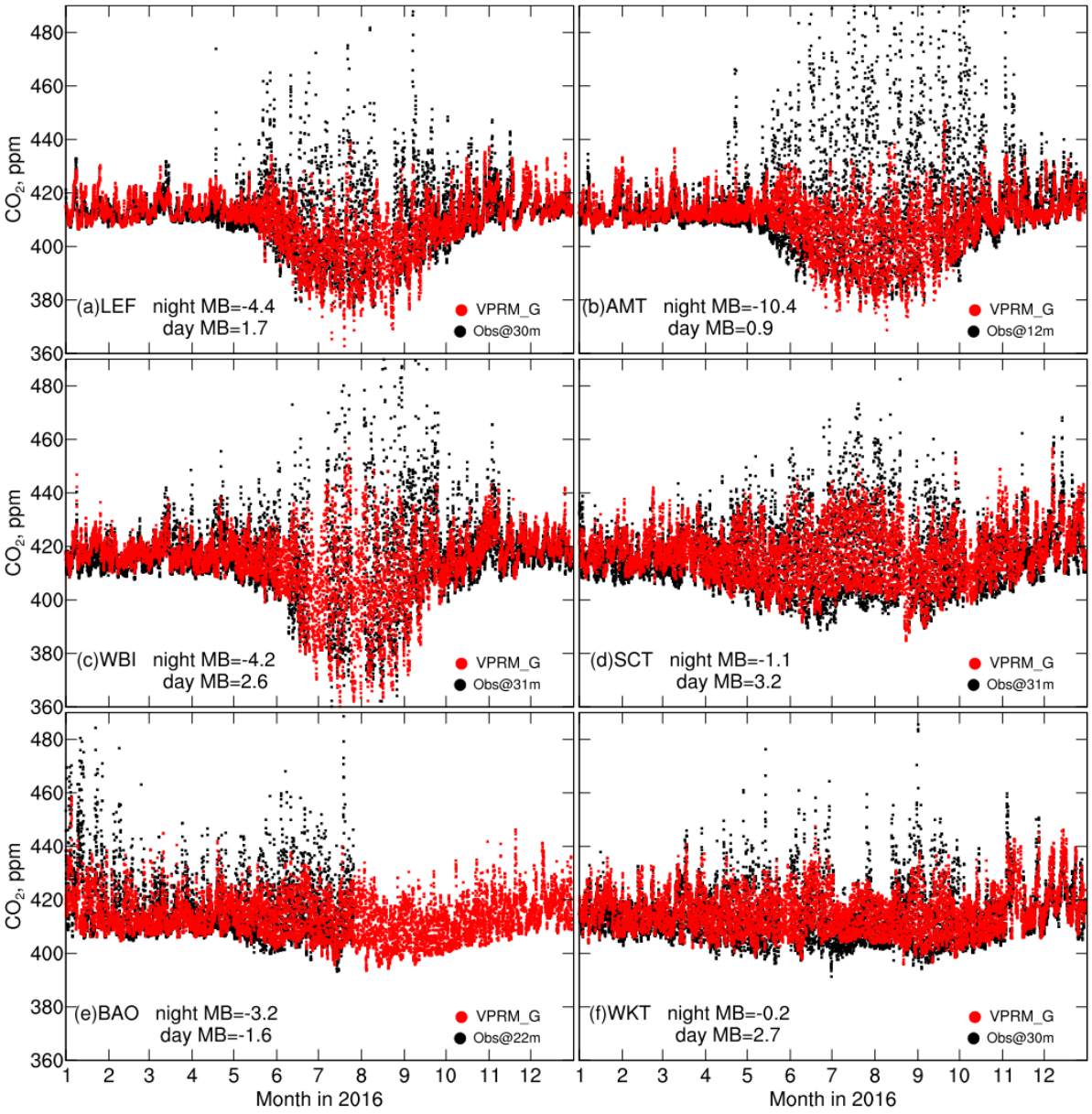

Figure 3. Near-surface CO_2 in 2016, observed at six NOAA tower sites and simulated by WRF-VPRM_G. Note that CO_2 is measured at different heights AGL at different towers, simulated values are extracted at the corresponding model height. Nighttime and daytime mean bias (MB) of CO_2 at each site is marked.

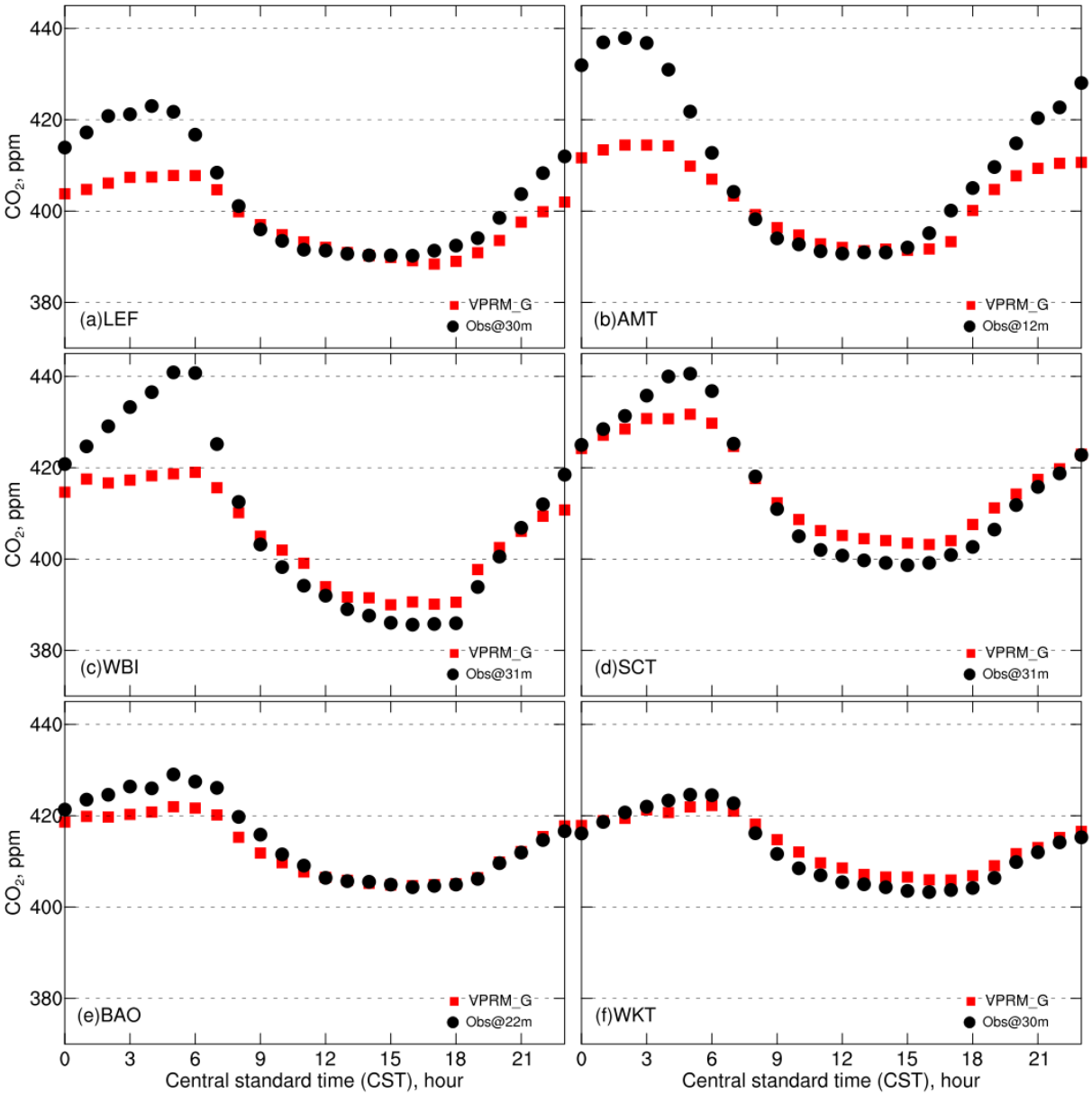

Figure 4. Median diurnal variation of near-surface CO_2 during growing season (June-September) in 2016, observed at six NOAA tower sites and simulated by WRF-VPRM_G. Note that CO_2 is measured at different heights AGL at different towers, simulated values are extracted at the corresponding model height.

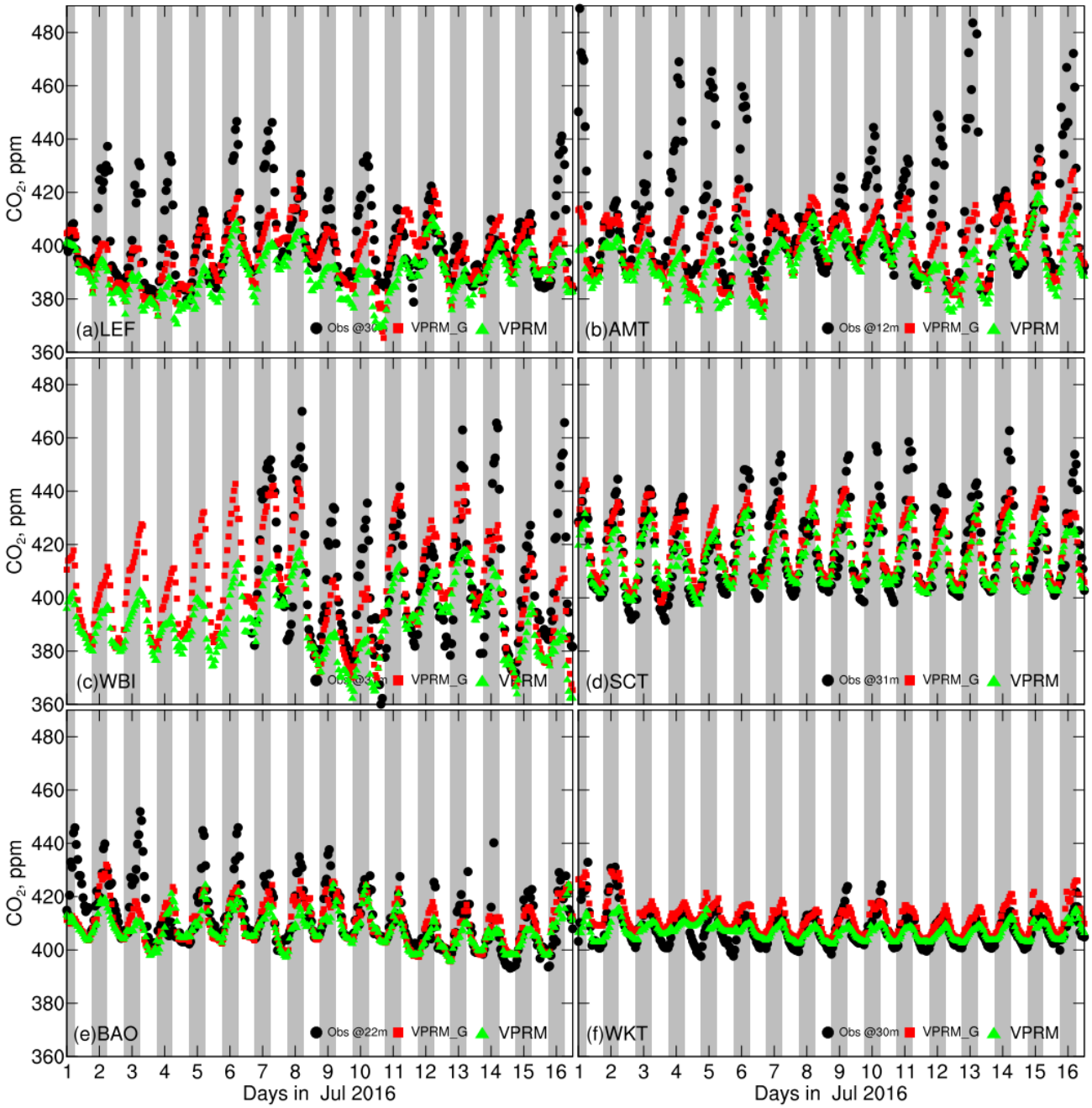

Figure 5. Near-surface CO_2 in first half of July 2016 (growing season for most sites), observed at six NOAA tower sites and simulated by WRF-VPRM_G in this study and WRF-VPRM in Hu et al. (2020). Nighttime is shaded.

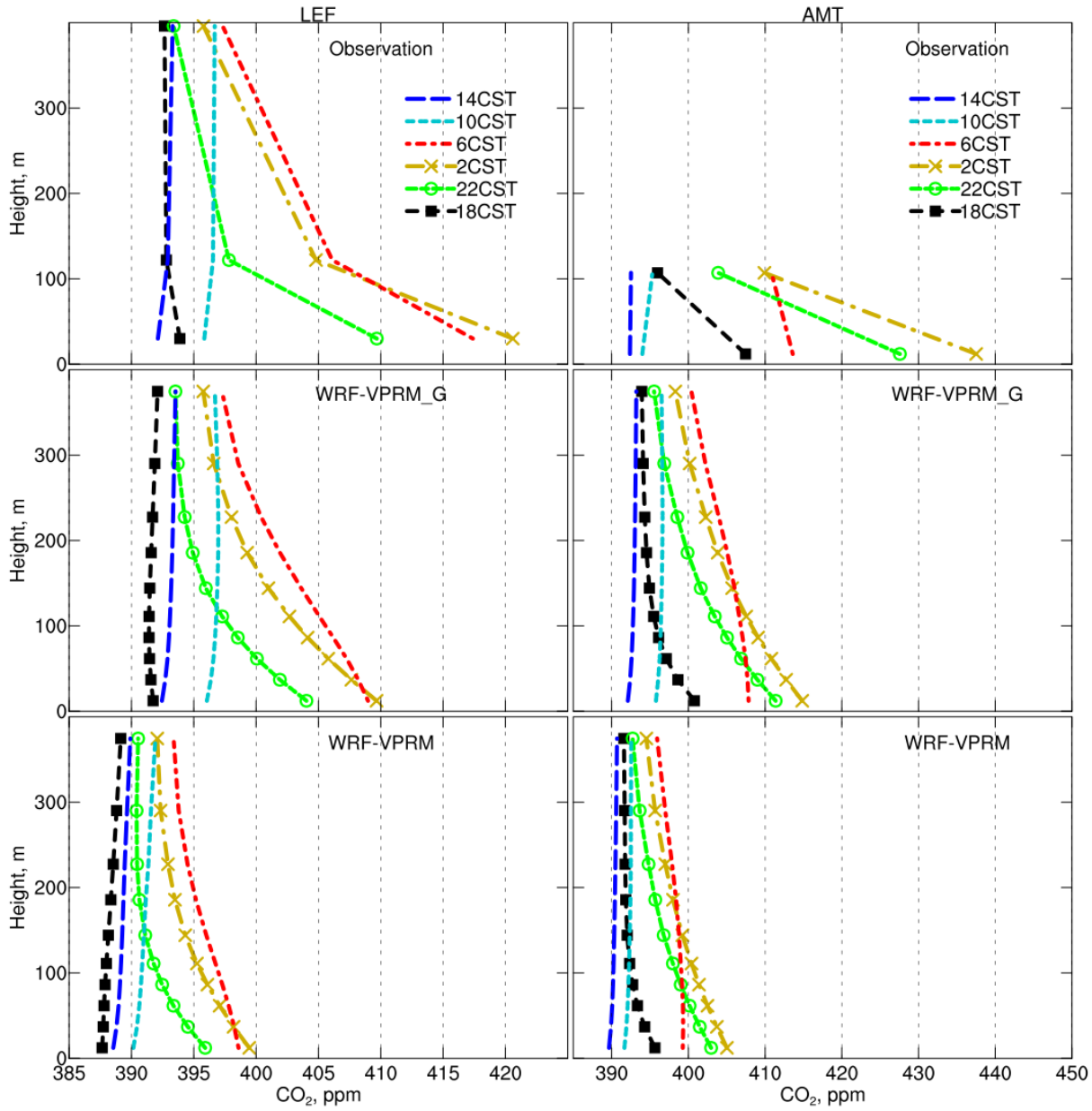

Figure 6. Mean CO_2 profiles in growing season (June-September) of 2016 (1st row) observed at (left) LEF and (right) AMT NOAA towers and simulated by (2nd row) WRF-VPRM_G in this study and (3rd row) WRF-VPRM in Hu et al. (2020).

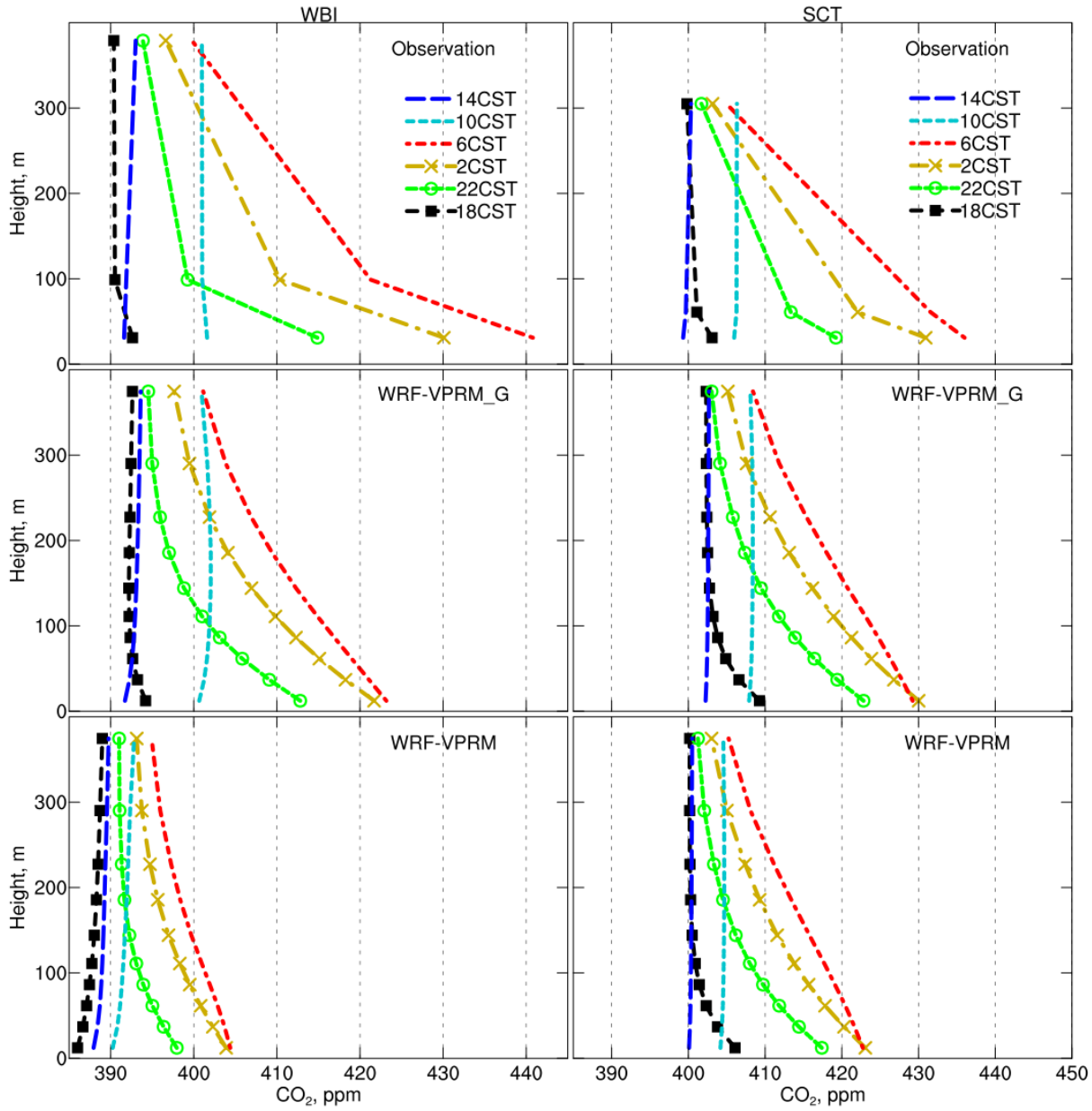

Figure 7. same as Figure 6, but at (left) WBI and (right) SCT NOAA towers.

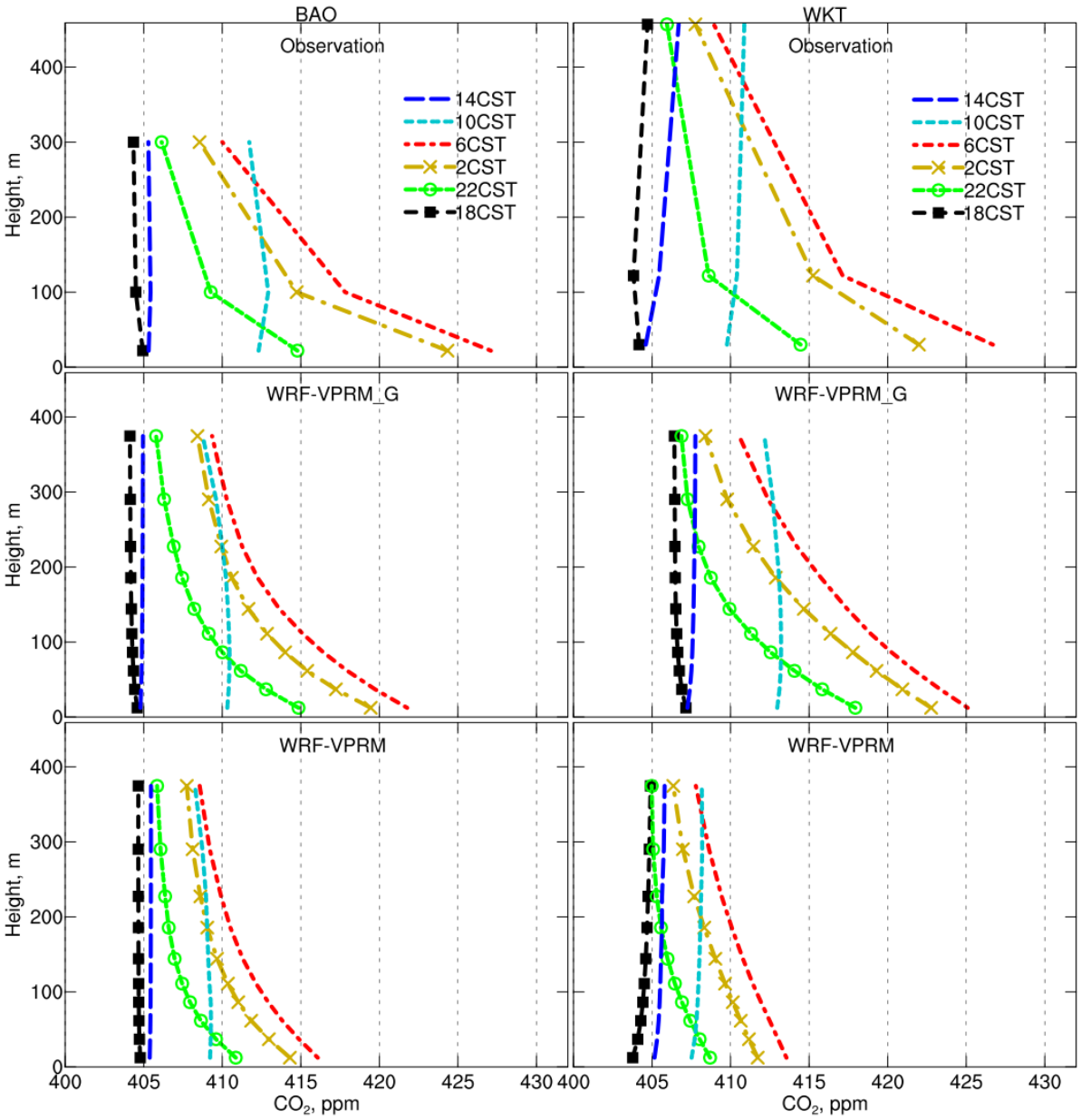

Figure 8. same as Figure 6, but at (left) BAO and (right) WKT NOAA towers.

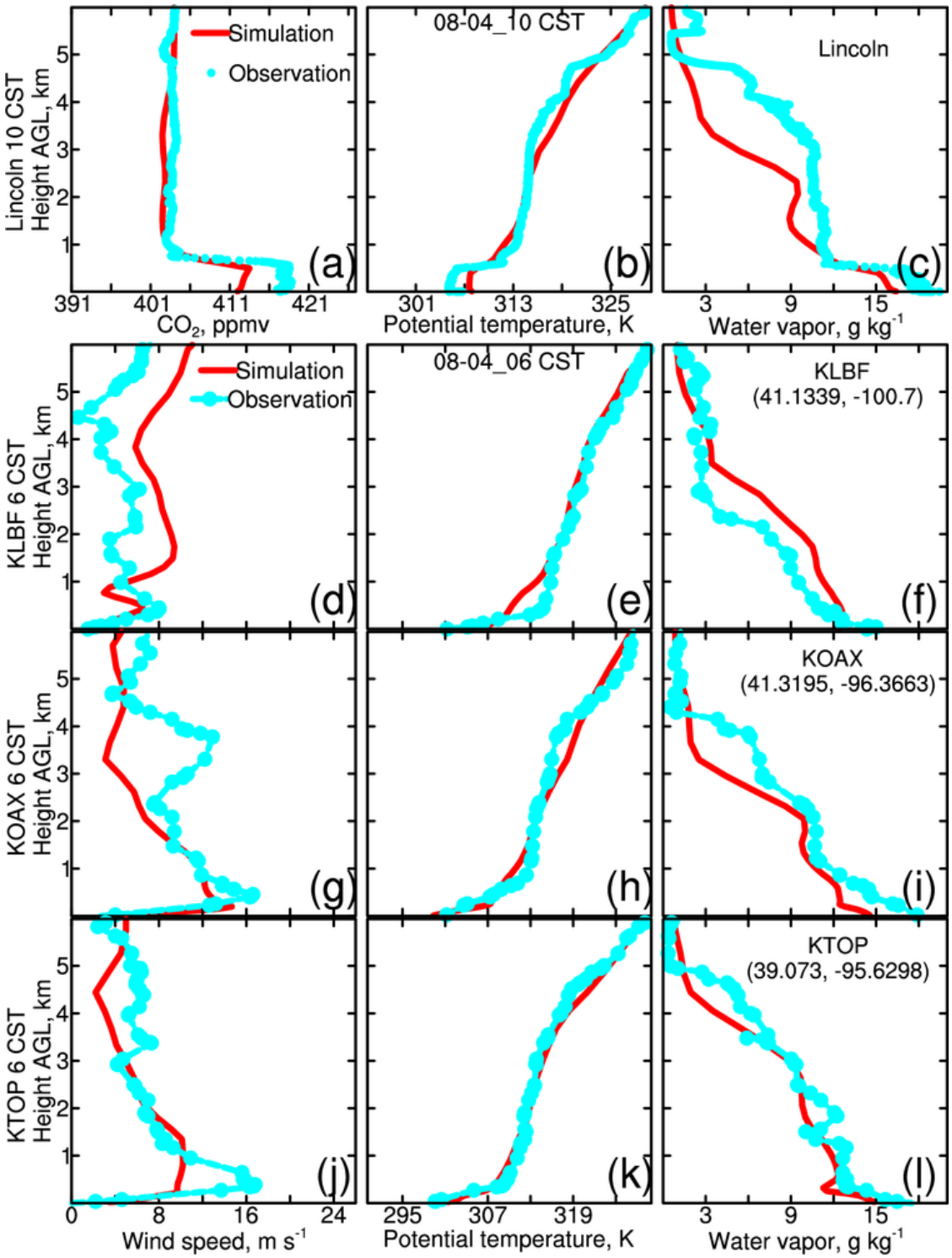

Figure 9. (1st row) Profiles of CO_2, potential temperature (θ), and water vapor mixing ratio simulated at 1000 CST and observed during the C130 ascending time between 1000-1015 CST on August 4 over the Lincoln airport (40.8367°N, 96.7619°W), and profiles of (left to right) wind speed, θ, and water vapor mixing ratio at 0600 CST on August 4 simulated and observed at sounding sites: (2nd-4th rows) KLBF, KOAX, and KTOP, which are marked on Fig. 10.

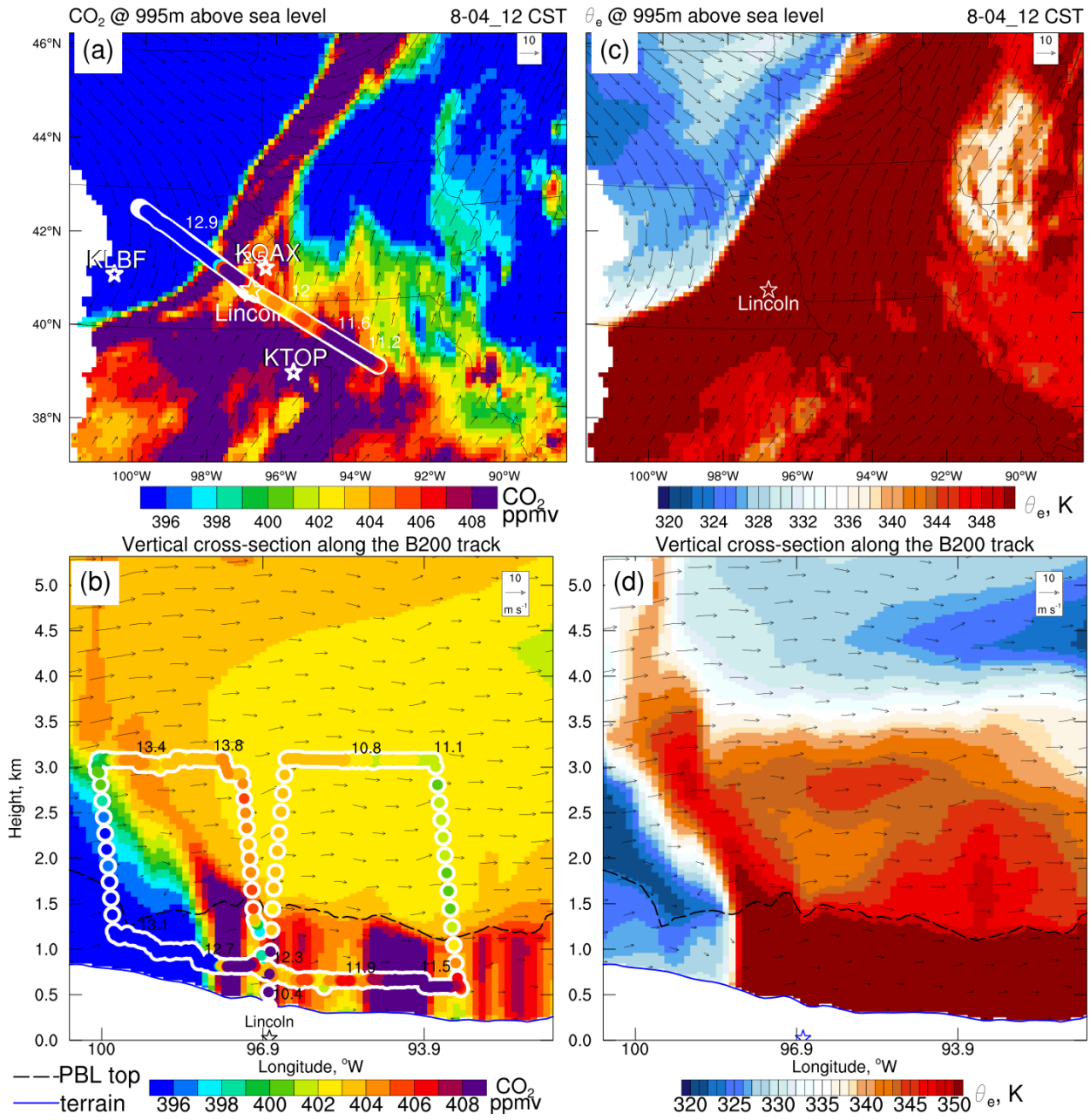

Figure 10. (a,c) horizontal (at ~995m above sea level) and (b,d) vertical cross sections of (left) CO_2 and (right) equivalent potential temperature (θ_e) through the B200 flight track at 1200 CST on August 4 simulated by WRF-VPRM_G, overlaid with B200 aircraft CO_2 data. Note that the flight path and CO_2 data are marked in panel a. The CST time is marked along the flight path.

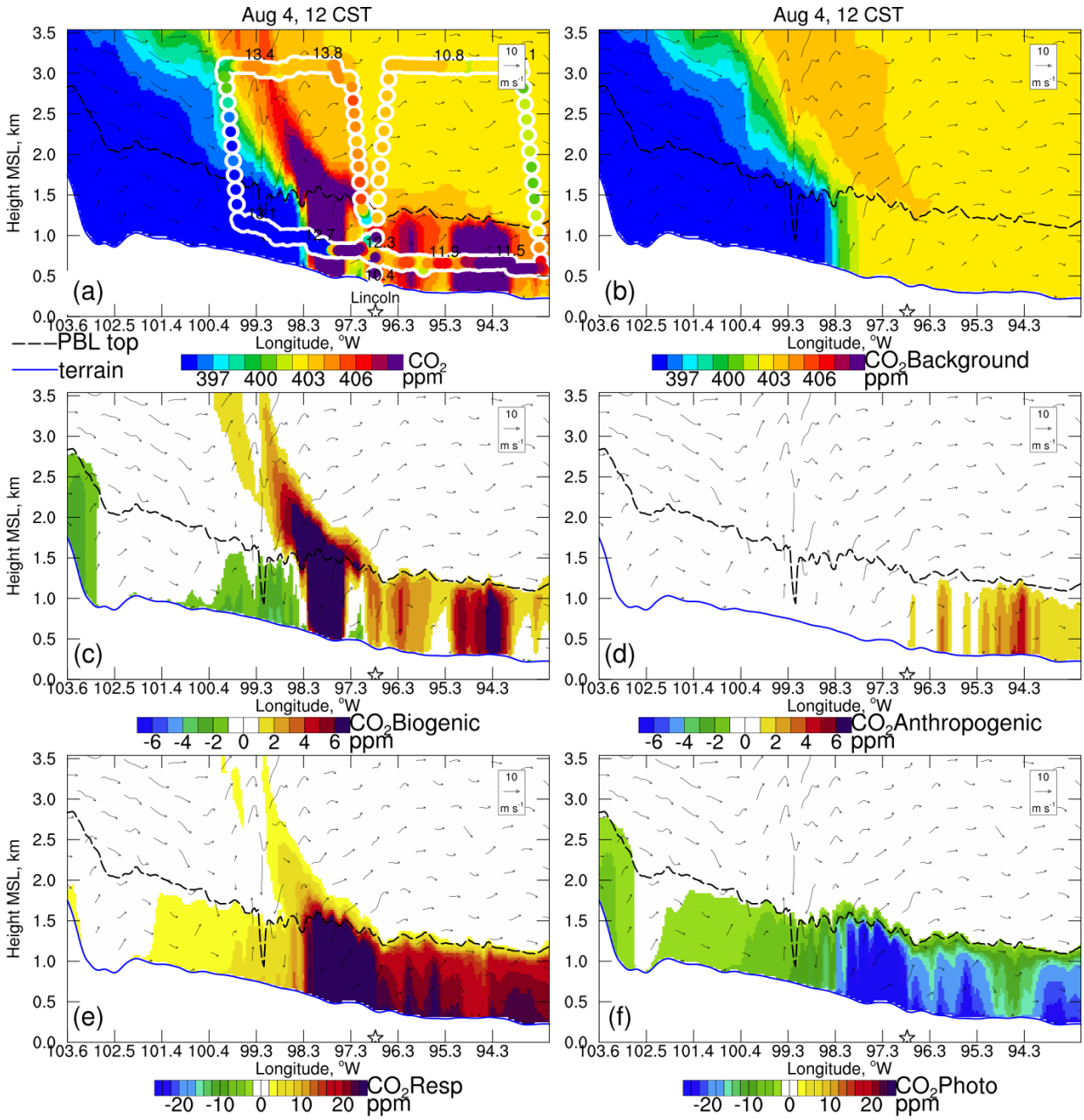

Figure 11. (a) vertical cross sections of total CO_2 through the B200 flight track at 1200 CST on August 4 simulated by WRF-VPRM_G in the nested inner domain, overlaid with B200 aircraft CO_2 data and (b-f) CO_2 components including background, biogenic, anthropogenic, respiration, and photosynthesis CO_2. Location of Lincoln is marked using a star on X-Axis.

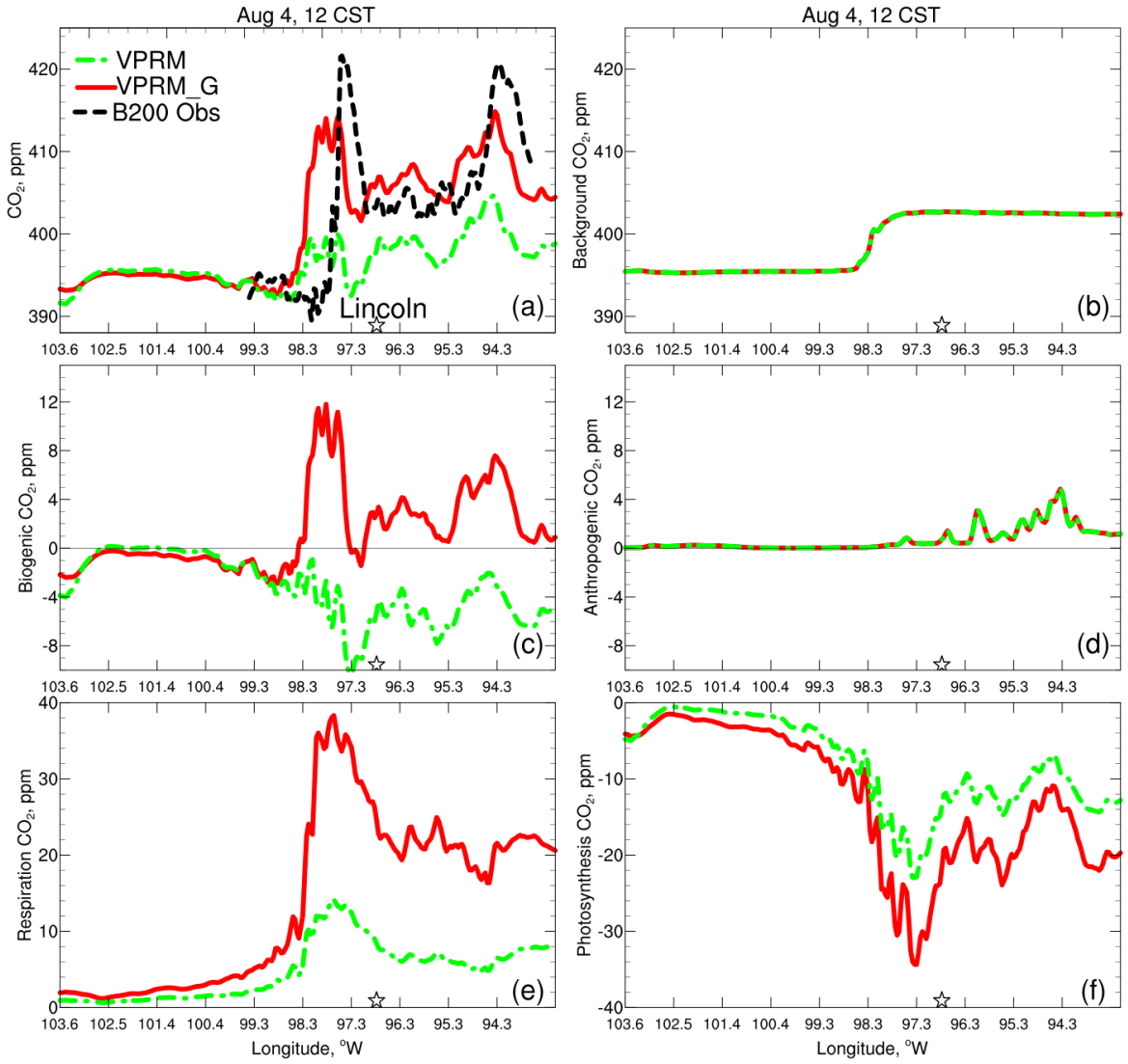

Figure 12. (a) Total CO_2 through the B200 flight track at 1200 CST on August 4 in the nested inner domain simulated by WRF-VPRM_G in this study and WRF-VPRM in Hu et al. (2020), along with B200 aircraft CO_2 data in the boundary layer during 11:20-13:10 CST and (b-f) simulated CO_2 components including background, biogenic, anthropogenic, respiration, and photosynthesis CO_2. Location of Lincoln is marked using a star on X-Axis.

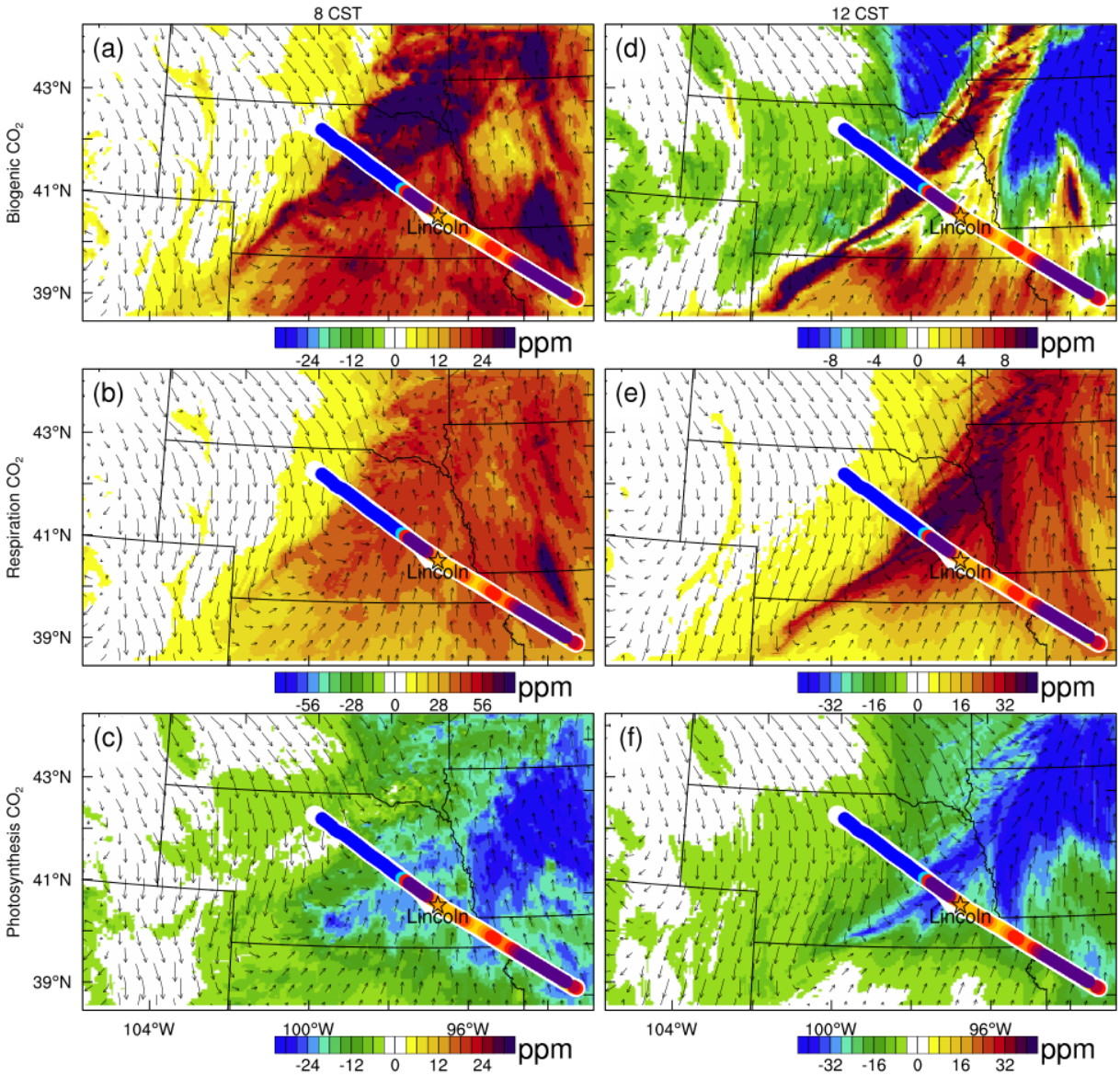

Figure 13. (top to bottom) Surface biogenic CO_2, respiration, and photosynthesis CO_2 at (a,b,c) 08 and (d,e,f) 12 CST. B200 aircraft CO_2 data in the boundary layer is overlaid for location reference.

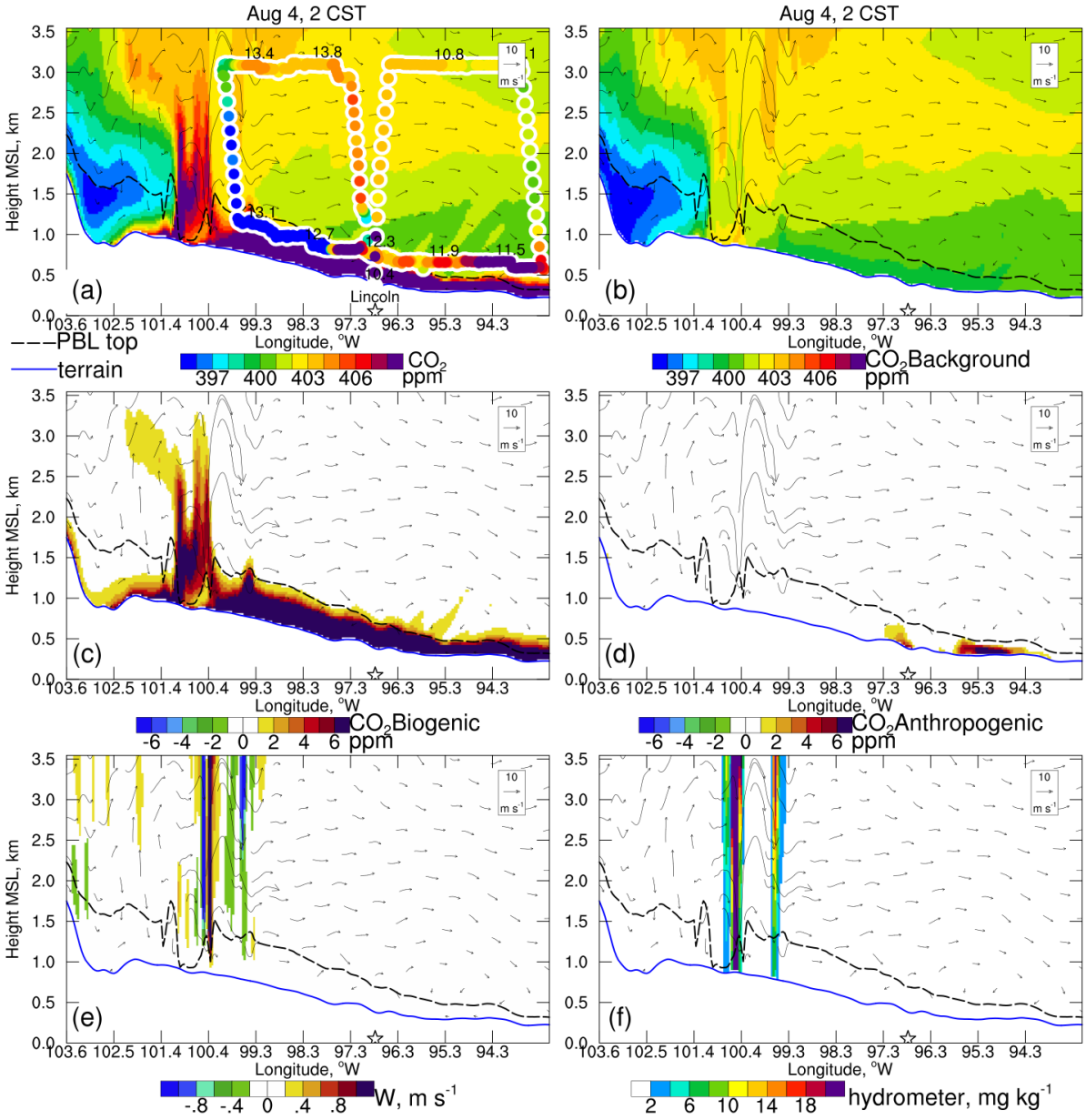

Figure 14. (a) vertical cross sections of total CO_2 through the B200 flight track at 0200 CST on August 4 simulated by WRF-VPRM_G in the nested inner domain, overlaid with B200 aircraft CO_2 data and (b-d) CO_2 components including background, biogenic, anthropogenic CO_2, (e-f) vertical velocity, and hydrometer mixing ratio.

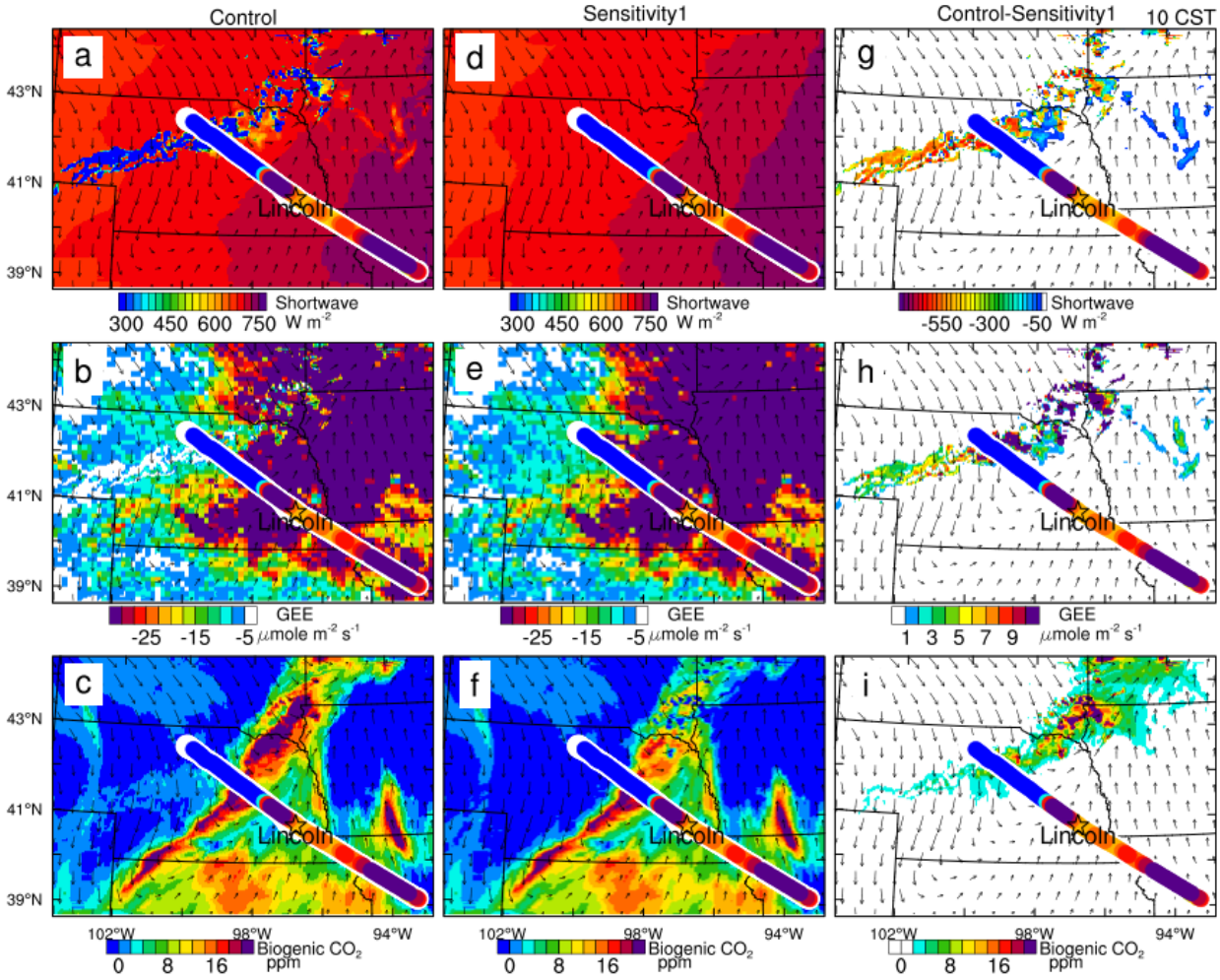

Figure 15. (top to bottom) surface short wave radiation, GEE, and biogenic CO_2 simulated by (left) control and (middle) the clear-sky-photosynthesis sensitivity simulation, and (right) their difference at 10 CST. B200 aircraft CO_2 data in the boundary layer at ~12 CST is overlaid.

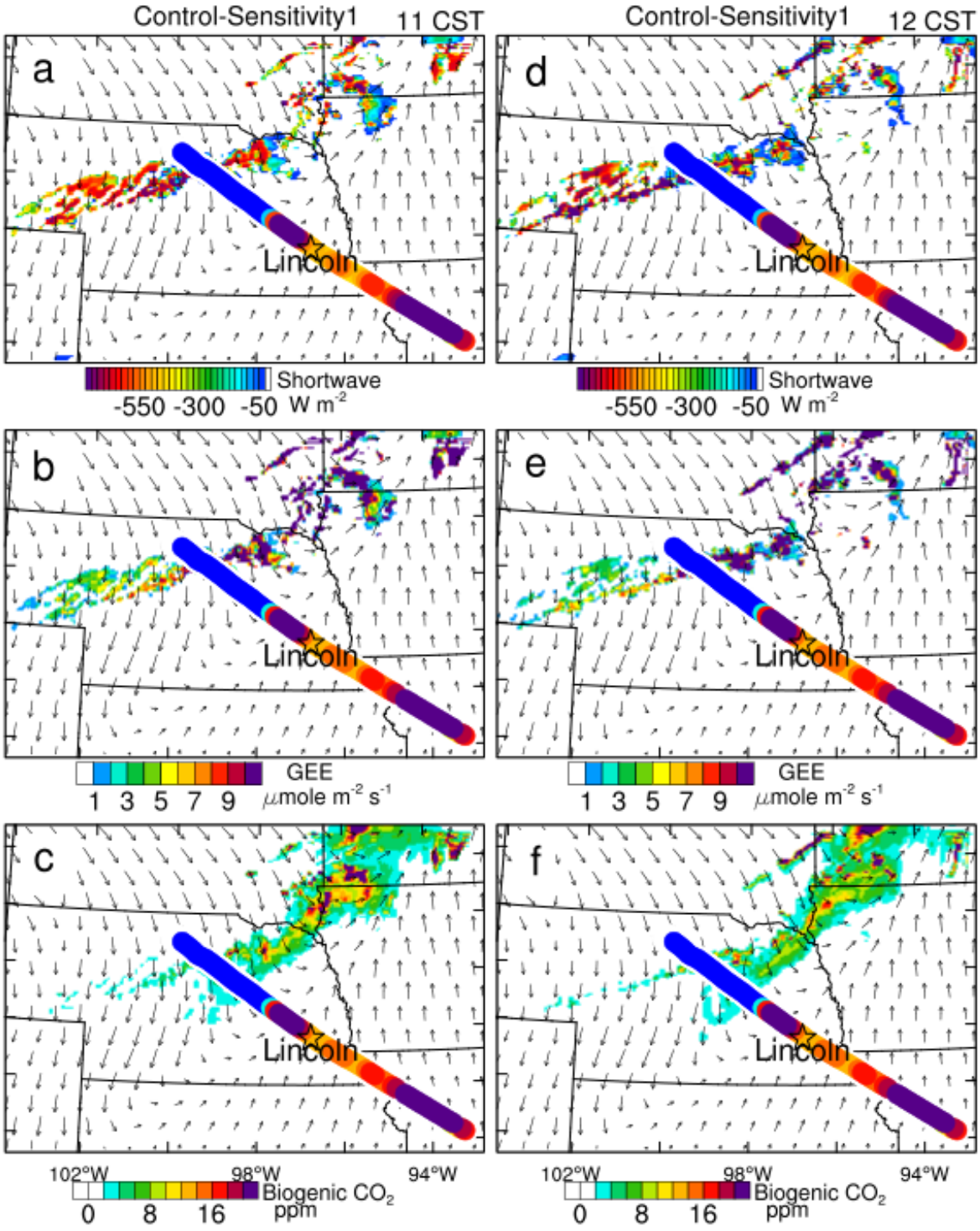

Figure 16. difference of (top to bottom) surface short wave radiation, GEE, and biogenic CO_2 simulated by the control and the clear-sky-photosynthesis sensitivity simulation, at (left) 11 CST and (right) 12 CST. B200 aircraft CO_2 data in the boundary layer at ~12 CST is overlaid.

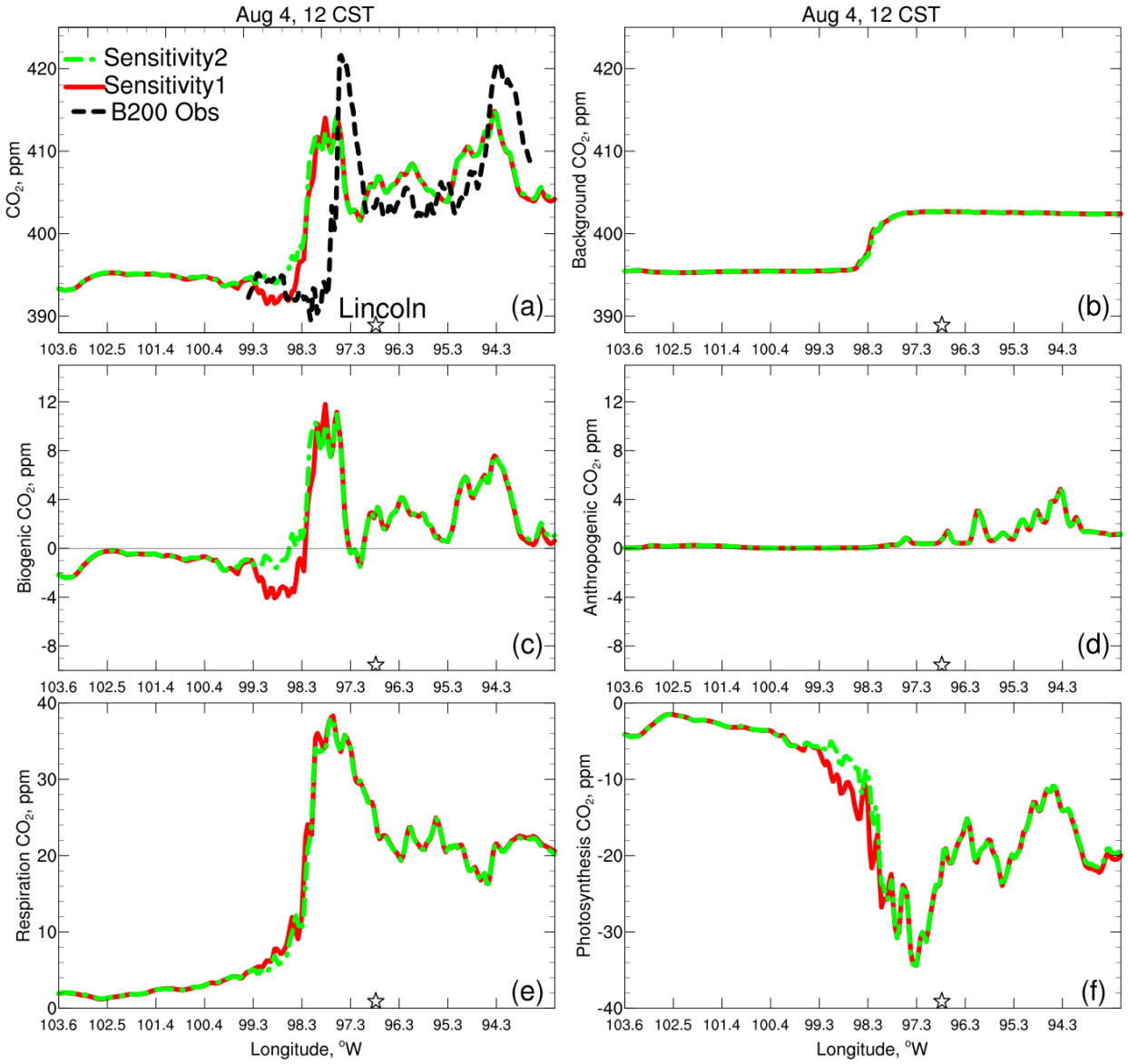

Figure 17. same as Figure 12, but simulated by the Sensitivity1 (clear-sky-photosynthesis) and Sensitivity2 (clear-sky-surface-energy) simulations.

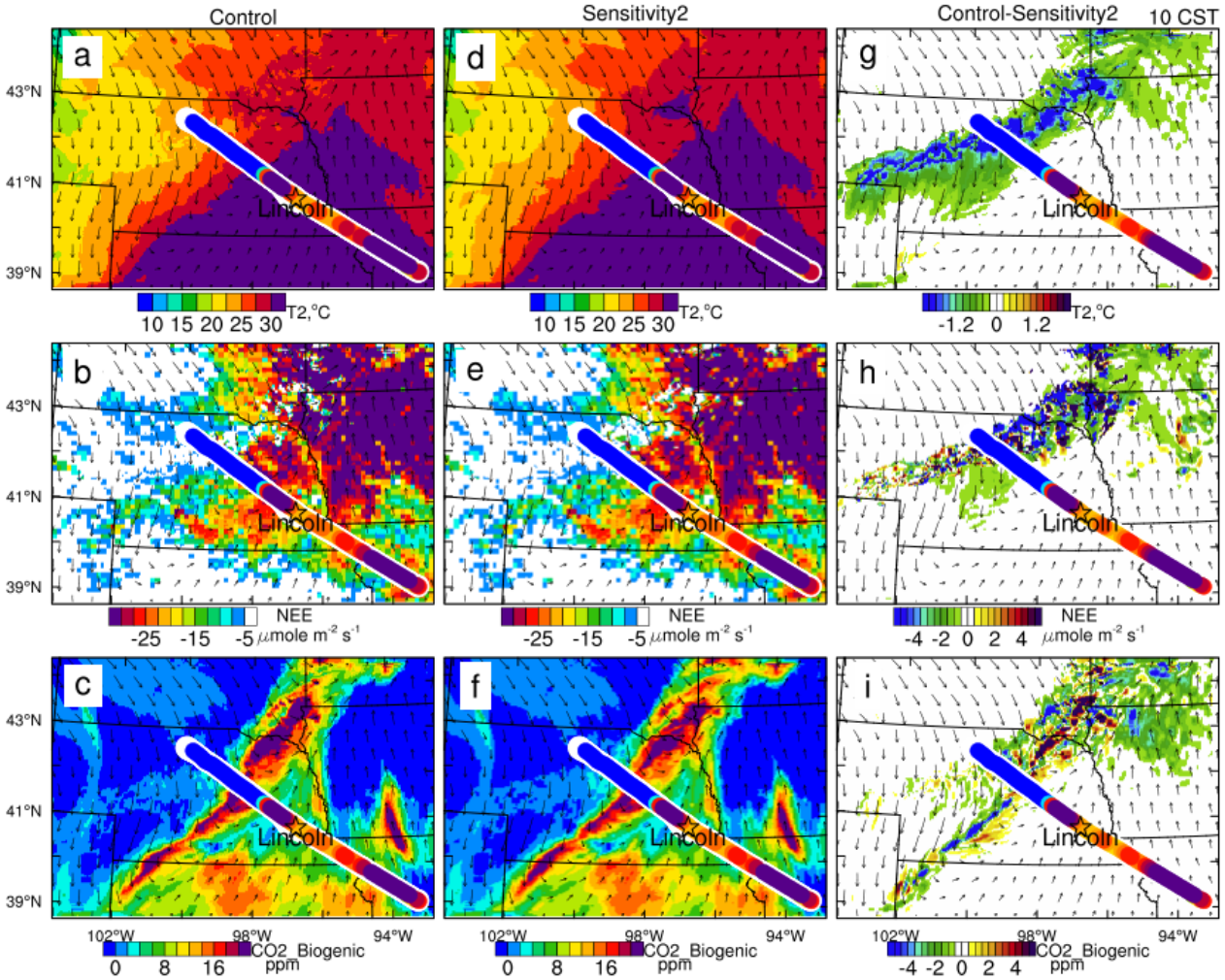

Figure 18. (top to bottom) temperature at 2 m AGL (T2), NEE, and biogenic CO_2 simulated by (left) control and (middle) the clear-sky-surface-energy sensitivity simulation, and (right) their difference at 10 CST. B200 aircraft CO_2 data in the boundary layer at ~12 CST is overlaid.